

Birth of a quasi-stationary black hole in an outcoupled Bose–Einstein condensate

J R M de Nova¹, D Guéry-Odelin², F Sols¹ and I Zapata¹

¹ Departamento de Física de Materiales, Universidad Complutense de Madrid, E-28040 Madrid, Spain

² Université de Toulouse, UPS, Laboratoire Collisions Agrégats Réactivité, IRSAMC, and CNRS, UMR 5589, F-31062 Toulouse, France

E-mail: jrmnova@fis.ucm.es

Received 28 July 2014, revised 7 November 2014

Accepted for publication 10 November 2014

Published 15 December 2014

New Journal of Physics **16** (2014) 123033

doi:[10.1088/1367-2630/16/12/123033](https://doi.org/10.1088/1367-2630/16/12/123033)

Abstract

We study the evolution of an initially confined atom condensate, which is progressively outcoupled by gradually lowering the confining barrier on one side. The goal is to identify protocols that best lead to a quasi-stationary sonic black hole separating regions of subsonic and supersonic flow. An optical lattice is found to be more efficient than a single barrier in yielding a long-time stationary flow. This is best achieved if the final conduction band is broad and its minimum is not much lower than the initial chemical potential. An optical lattice with a realistic Gaussian envelope yields similar results. We analytically prove and numerically check that, within a spatially coarse-grained description, the sonic horizon is bound to lie right at the envelope maximum. We derive an analytical formula for the Hawking temperature in that setup.

 Online supplementary data available from stacks.iop.org/njp/16/123033/mmedia

Keywords: Hawking radiation, optical lattice, atomtronics



Content from this work may be used under the terms of the [Creative Commons Attribution 3.0 licence](https://creativecommons.org/licenses/by/3.0/).

Any further distribution of this work must maintain attribution to the author(s) and the title of the work, journal citation and DOI.

1. Introduction

An attractive feature of Bose–Einstein condensates is their ability to provide a convenient way to investigate analog black-hole physics in the laboratory [1, 2]. Unruh noted [3, 4] that Hawking radiation in a cosmic black hole [5, 6] is an essentially kinematic effect that can be simulated in a quantum fluid. More specifically, it has been predicted that, for a quantum fluid passing through a sonic horizon (i.e., a subsonic–supersonic interface), phonons will be emitted into the subsonic region even at zero temperature [7–12].

A sonic black hole was recently realized in an accelerated Bose–Einstein condensate [13]. An alternative route towards the detection of Hawking radiation may be provided by a quasi-stationary horizon, which in principle can be achieved by allowing a large, confined condensate to emit in such a way that the coherent outgoing beam is dilute and fast enough to be supersonic [11, 14–16]. The hope is that the elusive Hawking radiation will be less difficult to detect unambiguously in such quasi-stationary transport scenarios. In particular, recent research has addressed the possibility of detecting the spontaneous Hawking radiation above the stimulated signal [17–19]. Experimental evidence of stimulated Hawking radiation was recently found in a black-hole laser setup [20].

This paper aims to explore the actual attainability of the steady-state regime. Within a mean-field approximation, we investigate the dynamics of an initially confined condensate that begins to leak as the height of one of the confining barriers is driven from an essentially infinite to a finite value that permits a gentle yet appreciable flow of coherently outcoupled atoms. An alternative route to a quasi-stationary black-hole configuration has been proposed for atom [21] and polariton [22] condensates, based on the idea of throwing the condensate onto a localized obstacle such as a potential barrier. In the present work, we focus on a finite-sized condensate and on cases where the increasingly transparent potential is formed not by a single [16] or double [15] barrier, but by an extended optical lattice, because the latter scenario seems more suitable for the achievement of quasi-stationary flow within this deconfinement scheme, as we will show later. We will see that close-to-ideal stationary flow within the permitted energy bands is achievable under realistic opening protocols.

The present mean-field study aims to identify transport scenarios that offer the potential hopes for detecting Hawking radiation in the future. More conclusive predictions about the detectability of spontaneous radiation will require a study of the time-dependent Bogoliubov-de Gennes (BdG) equations, which should show us the actual intensity of the expected spontaneous radiation. This task is left for a future study.

In addition to the motivation of realizing gravitational analogs, the achievement of stationary transport scenarios is of general interest to the investigation of atom quantum transport, in the case of both bosons [23–28] and fermions [29, 30], within the emergent field of atomtronics.

This paper is arranged as follows. Section 2 presents the model for the gradual reduction of the optical lattice amplitude that we will investigate. After some preliminary remarks in section 3, we present the main numerical results, along with some theoretical arguments (that help to understand the observed trends) in section 4. The second part of that section describes the achieved quasi-stationary regime. Section 5 addresses the more realistic case of an optical lattice with a Gaussian envelope. Interestingly, we find that the horizon lies at the maximum of the envelope, and we give a theoretical explanation of that fact. The main conclusions are summarized in section 6. Appendix A provides a detailed description of the initial state of the

condensate as it exists before the deconfinement procedure begins. Appendix B discusses some properties of Bloch waves in the presence of the nonlinearities that account for the interaction. Appendix C presents a perturbative treatment of the interaction. Finally, appendix D describes the numerical method of integration and the use of absorbing boundary conditions.

2. The model

In this work, we study the outcoupling of a one-dimensional (1D) Bose–Einstein condensate through a finite-size repulsive optical lattice whose intensity is gradually lowered in such a way that, within a finite time frame, the periodic barrier shifts from a regime of practical confinement to one of full transparency within certain atom energy bands. We focus on the mean-field dynamics (i.e., we only consider the evolution of the condensate wave function, leaving the dynamics of quasi-particles for a future study). We restrict our present study to a quasi-1D model. The time-dependent condensate wave function, $\Psi(x, t)$, obeys the Gross–Pitaevskii (GP) equation [31, 32]:

$$i\hbar \frac{\partial \Psi(x, t)}{\partial t} = \left[-\frac{\hbar^2}{2m} \partial_x^2 + V(x, t) + g |\Psi(x, t)|^2 \right] \Psi(x, t), \quad (1)$$

where m is the atom mass and $V(x, t)$ is the time-dependent optical lattice potential. The effective 1D coupling constant, $g = 2\hbar\omega_{\text{tr}}a_s$ (where a_s is the s -wave scattering length), is the relevant interaction strength in a setup where only the ground state of a confining transverse harmonic oscillator of frequency $\omega_{\text{tr}}/2\pi$ is populated. This is the 1D mean-field regime, characterized by the condition $\rho a_s \ll 1$, where $\rho(x, t) = |\Psi(x, t)|^2$ [33, 34]. At the same time, $\rho a_{\text{tr}}^2/a_s \gg 1$ (with a_{tr} as the transverse oscillator length) must be satisfied to stay away from the Tonks-Girardeau regime [33, 35, 36]. Taking the initial bulk density, n_0 , as a typical value for the density, we can realistically set (see section 4) $n_0 a_s \sim 10^{-1}$ and $n_0 a_{\text{tr}}^2/a_s \sim 10^3$, from which we conclude that we are safely in the 1D mean-field regime.

Equation (1) conserves the total particle number, N , as given by the normalization condition

$$N = \int dx |\Psi(x, t)|^2. \quad (2)$$

The condensate density is nonzero only for $x > 0$, because at all times we assume a sufficiently high barrier at $x = 0$, which is simply implemented via the hard-wall boundary condition, $\Psi(0, t) = 0$.

Initially (at times $t < 0$), we consider an equilibrium condensate made of N atoms occupying the region $0 < x \lesssim L$. Thus, $n_0 \simeq N/L$ is the initial atom density, which is defined more precisely below. We also introduce an optical lattice that spans the region $L \lesssim x \lesssim L + L_{\text{lat}}$, whose initial amplitude, V_0 , is large enough that particle tunneling through the lattice is practically forbidden. The initial wave function is stationary, $\Psi(x, t) = e^{-i\mu_0 t/\hbar} \Psi(x)$, with $\Psi(x)$ satisfying the time-independent GP equation

$$\left[-\frac{\hbar^2}{2m} \partial_x^2 - \mu_0 + V(x, 0) + g |\Psi(x)|^2 \right] \Psi(x) = 0. \quad (3)$$

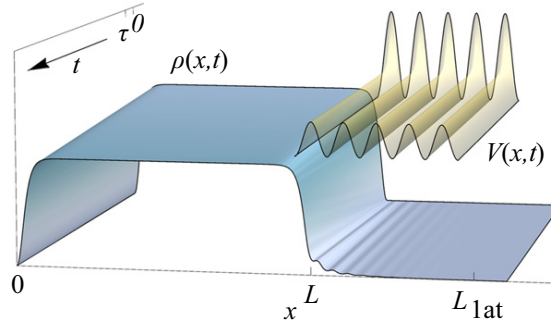


Figure 1. Schematic representation of the emitting condensate setup studied in this article. Within the ideal lattice scenario, hard-wall boundary conditions are assumed at $x = 0$, and an optical lattice lies in the region $L < x < L_{\text{lat}}$ with a time-dependent amplitude such that the potential, $V(x, t)$ (represented by the semi-transparent yellow surface over the $x - t$ plane), evolves from strongly to moderately confining. The resulting time-dependent density profile, $n(x, t)$, is represented by the grey-blue surface. The vertical axis gives the density in some (unimportant) units. The surface, $V(x, t)$, is uplifted to provide a better vision of $n(x, t)$. Some parameters defined in the main text are indicated. The trend towards a long-time quasi-stationary flow regime can be qualitatively observed.

The initial chemical potential, μ_0 , is determined by the normalization condition (2). The initial healing length is defined as $\xi_0 \equiv \sqrt{\hbar^2/mgn_0}$, where $n_0 \equiv \mu_0/g$. Further details on the initial condensate are given in appendix A. At time $t = 0$, the optical lattice intensity starts to decrease and atoms begin to escape toward the region $x \gtrsim L + L_{\text{lat}}$, where the potential is assumed to be negligible. On fairly general grounds [15, 34, 37], we can expect the flow beyond the optical lattice to be supersonic.

We assume that the optical lattice is made of two fixed phase lasers of wavelength λ , and whose wave vectors form an angle, θ [38, 39]. The time-dependent optical lattice potential is chosen so that in the lattice region (defined by $L - \frac{d}{2} \leq x \leq L - \frac{d}{2} + L_{\text{lat}}$) and for times $t \geq 0$,

$$\begin{aligned} V(x, t) &= V(t) \cos^2[k_L(x - L)] \\ V(t) &= V_\infty + (V_0 - V_\infty)e^{-t/\tau}, \end{aligned} \quad (4)$$

where $k_L = \pi/d$ and $d = \lambda/[2 \sin(\theta/2)]$ is the lattice period, while $V(x, t) = 0$ everywhere else.

The potential profile in equation (4) is somewhat idealized. A more realistic choice should include a Gaussian envelope. For simplicity, we choose to start by considering a flat-envelope optical lattice, where Bloch's theorem can be invoked with reasonable confidence. We will see that, remarkably, essentially the same results are obtained when a more realistic Gaussian envelope is used. A sketch of the time-dependent, flat-envelope optical potential and the resulting condensate flow is presented in figure 1.

3. Preliminary remarks

We note that the time-dependent amplitude, $V(t)$, evolves from $V_0 \gg \mu_0$ at $t \leq 0$ to $V_\infty \gtrsim \mu_0$ for $t \gg \tau$. The asymptotic behavior is determined by the initial parameters of the condensate

(N, g, L) , the specific form of the final potential (V_∞, d) , and the barrier-lowering time scale (τ) . The initial potential amplitude, V_0 , plays almost no role, provided that it is sufficiently large. More precisely, the condition of initial confinement requires μ_0 to lie well below the lowest conduction band of the initial optical lattice potential. On the other hand, the properties of the final steady state are insensitive to τ unless τ is very small (see subsection 4.1.2).

The main goal of this work is to identify the barrier-lowering protocol that best leads to a regime of quasi-stationary outcoupled flow, by which we mean a flow regime characterized by parameters that vary slowly in time in a sense that we will specify later. For space dependence in that regime, we require the density to be as uniform as possible in the region $0 < x \lesssim L$.

In the supersonic region ($x \gtrsim L + L_{\text{lat}}$), we also want a uniform flow profile, even though this will be more difficult to achieve due to the low density. However, disturbances in the supersonic region should not affect the spectrum of the part of the Hawking radiation that is emitted into the subsonic region. On the other hand, in the optical lattice region, the flow should be as close as possible to that of a propagating Bloch wave. At the boundary between these two regions, large gradients of the flow speed and density are likely to occur, but the current density should remain essentially uniform.

In what follows, when we refer to bands, we mean the Schrödinger (noninteracting) bands, unless specified otherwise. Bands in a nonlinear context are discussed in appendices B and C. We will see that in virtually all cases, the relevant properties of the optical lattice are determined by its lowest band, provided the lattice is sufficiently long. An important result is that, due to the finite size of the subsonic reservoir, the quasi-stationary flow is formed only when the space-averaged chemical potential lands at a value slightly above the bottom of the lowest lattice band. Because the local chemical potential is approximately uniform along the structure, this implies that the density is small almost everywhere in the optical lattice region. As a consequence, the interaction term can be neglected, since $g |\Psi(x, t)|^2 \ll (\hbar k_L)^2/m$; see appendix B for details. In the noninteracting regime, equation (1) becomes the usual Schrödinger equation, which for a sinusoidal potential can be transformed into a Mathieu's equation [40].

The structure of the final bands can be characterized by the dimensionless parameter

$$v \equiv mV_\infty/8\hbar^2k_L^2. \quad (5)$$

The nearly-free atom regime occurs when $v \ll 1$. Then bands are wide and gaps are narrow. By contrast, in the tight-binding regime ($v \gg 1$), bands are narrow and widely spaced. Since $v \propto V_\infty d^2$, the band structure can be modified by changing the lattice amplitude or its spacing.

4. Ideal optical lattice

In this work, the unit length is the initial bulk healing length, ξ_0 , defined in section 2. Accordingly, velocities are measured in units of the sound speed, $c_0 \equiv \sqrt{gn_0/m}$, and times are measured in units of $t_0 \equiv \xi_0/c_0$. Energies are expressed in units of the initial chemical potential, $\mu_0 = mc_0^2$. Quasi-1D condensates of ^{87}Rb are typically made of $N \sim 10^4 - 10^7$ atoms and have a transverse trapping frequency of $\omega_{\text{tr}} \sim 2\pi \times 10^3$ Hz and a confinement length of $L \sim 10-400 \mu\text{m}$. The optical lattice periodicity is bounded from below, $d > \lambda/2$ nm, for geometrical reasons. The value of lambda is chosen to be sufficiently far from the resonance to avoid any spontaneous emission, and on the blue-side of the resonance to produce a repulsive potential

($\lambda < 780$ nm for rubidium atoms). The simulations are run up to times $t \sim 10^4$ – $10^5 t_0$. As $t_0 = (2n_0 a_s \omega_{\text{tr}})^{-1} \sim 10^{-4}$ s, then $t \sim 1$ – 10 s for our simulations, which is on the order of the mean lifetime of this type of condensate.

In the simulations, we use a numerical scheme based on the Crank–Nicolson method to integrate the time-dependent GP equation (1). Hard-wall boundary conditions are assumed at $x = 0$. At the other end of the finite-size computational grid (located at $x = L_g$, with L_g as the total length of the grid), we use absorbing boundary conditions. L_g is taken so that the final point of the grid is sufficiently far from the end of the optical lattice for the supersonic region to be clearly observed. Further details of the numerical method are given in appendix D.

4.1. Analysis of the simulations

To characterize the quasi-stationary regime, we use the local chemical potential defined as

$$\mu(x, t) \equiv -\frac{\hbar^2}{2m} \frac{\partial^2 \Psi(x, t) / \partial x^2}{\Psi(x, t)} + V(x, t) + g |\Psi(x, t)|^2, \quad (6)$$

which can be complex. For a stationary solution, $\Psi(x, t) = e^{-i\mu t/\hbar} \Psi(x)$, one has $\mu(x, t) = \mu$, real and independent of (x, t) . The current,

$$j(x, t) = -\frac{i\hbar}{2m} \left(\Psi^* \frac{\partial \Psi}{\partial x} - \Psi \frac{\partial \Psi^*}{\partial x} \right) \quad (7)$$

is also independent of (x, t) for a stationary solution, as dictated by the continuity equation, $\partial_t \rho + \partial_x j = 0$. In the quasi-stationary regime, the uniformity of $j(x, t)$ is impossible to fulfill strictly, because the current is zero at $x = 0$, while the emitted atoms carry a nonzero current. Thus, there must be a current gradient and, by the continuity equation, the density has to be time dependent. However, the hope is that, in the quasi-stationary regime, this time dependence is weak because the condensate leak is slow.

On the other hand, we can expect that, in the quasi-stationary regime, $\mu(x, t)$ is a sufficiently uniform function, with small spatial variations around its space-averaged mean value. To check this expectation in a quantitative manner, we introduce the space-averaged chemical potential, $\bar{\mu}(t)$, together with an appropriate measure of its relative spatial fluctuation spread, $\sigma(t)$:

$$\bar{\mu}(t) \equiv \frac{\int_0^{L_g} dx \rho(x, t) \mu(x, t)}{\int_0^{L_g} dx \rho(x, t)}$$

$$\sigma(t) \equiv \frac{1}{\bar{\mu}(t)} \left[\frac{\int_0^{L_g} dx \rho(x, t) |\mu(x, t) - \bar{\mu}(t)|^2}{\int_0^{L_g} dx \rho(x, t)} \right]^{\frac{1}{2}}. \quad (8)$$

We recall that $\mu(x, t)$ and $\bar{\mu}(t)$ can be complex. A nonzero imaginary part of $\mu(x, t)$ reflects a leaking condensate, as revealed by the local relation

$$\frac{\partial \rho}{\partial t} = \frac{2}{\hbar} \rho \operatorname{Im} \mu. \quad (9)$$

Accordingly, we can define and compute the emission rate per particle as

$$\Gamma(t) \equiv \frac{j(L_g, t)}{\int_0^{L_g} dx \rho(x, t)} = -\frac{2}{\hbar} \operatorname{Im} \bar{\mu}(t), \quad (10)$$

where the continuity equation has been used. The spatial average of the time-dependent chemical potential [see equation (8)] is mostly determined by the subsonic region, where $\mu(x, t) \simeq g\rho(x, t)$.

A further rescaling of the condensate wave function, $\Psi(x, t) \rightarrow \sqrt{n_0} \Psi(x, t)$, more neatly reveals the intrinsic parameters governing the system. Once the healing length, ξ_0 , is given, only L/ξ_0 , d/ξ_0 , τ/t_0 , V_∞/mc_0^2 , and $n_{\text{osc}} \equiv L_{\text{lat}}/d$ (number of oscillations in the optical lattice) are relevant to the problem. We have already noted that V_0 plays almost no role in the limit $V_0 \gg \mu_0$. We find that, for the pertinent experimental ranges, namely $L \sim 10\text{--}400 \mu\text{m}$, variations of L/ξ_0 have little effect on the properties of the quasi-stationary regime. We have noted that they have a small influence on the time needed to achieve the desired quasi-stationarity, which grows weakly with the initial size of the condensate. A similar point can be made about n_{osc} , which becomes unimportant when it lies in the range $n_{\text{osc}} \sim 15\text{--}100$. The (relatively small) effect of increasing n_{osc} even further is that there are more spatial fluctuations in the chemical potential, for two reasons: the optical lattice tends to host larger $\mu(x, t)$ spatial fluctuations than the subsonic zone because of atomic reflections across the wells, an effect that is enhanced for larger optical lattices; and the larger the lattice, the bigger its contribution to the average chemical potential and its fluctuations.

In summary, except for the above remarks, only the parameters d/ξ_0 , τ/t_0 , V_∞/mc_0^2 , have a noticeable effect on the transport properties of the system under study.

4.1.1. Role of the final band structure. As previously noted, the combination of d and V_∞ fixes the final band structure. Figure 2 shows the various possible scenarios, depending on the long-time width and position of the lowest band with respect to the initial chemical potential, μ_0 . The band structure is computed numerically. The desired steadiness of the long-time behavior improves with the width of the band, as the first row in figure 2 reveals. In figure 2(a), a favorable case (wide band) is presented and compared with a less favorable case in figure 2(b), which has the same conduction band minimum but a narrower band. After a short transient, a comparison of the relative chemical-potential standard deviation, $\sigma(t)$, as defined in equation (8) and plotted in the graph, shows a clear advantage in the use of wider bands. For instance, in figure 2(a), $\sigma(t) \sim 10^{-4}$ in the stationary (long-time) regime, about 10 times smaller than in figure 2(b).

After a transition time of order $\sim 5000t_0$, all the characteristic magnitudes of the system shown in figure 2(a) vary slowly enough in time to properly view the resulting flow regime as quasi-stationary. In fact, the leak is so slow that other processes that limit the lifetime of the condensate (such as condensate decay due to inelastic collisions) operate on a shorter time scale.

If the chemical potential reaches and goes below the bottom of the conducting band in a relatively short time, then a transition occurs to an essentially confined situation where the leak

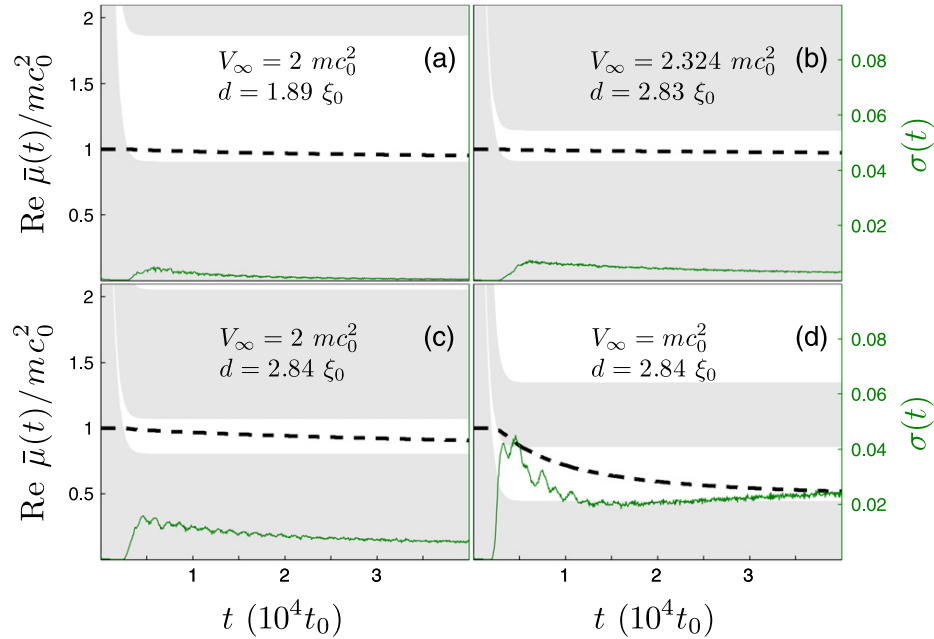


Figure 2. Time evolution of the real part of the space-averaged chemical potential, $\bar{\mu}(t)$ (black dashed line), and its fluctuation spread, $\sigma(t)$ (green solid line), both defined in equation (8). The gap and conduction band of the instantaneous band structure, which was computed from the potential equation (4) are indicated, respectively, by grey and white backgrounds. All graphs are computed with $\tau = 500 t_0$, $L = 400 \mu\text{m}$, $n_{\text{osc}} = 30$, $N = 10^4$, and $\omega_{\text{tr}} = 2\pi \times 4 \text{ kHz}$, which yields $n_0 = 25 \mu\text{m}^{-1}$ and $\xi_0 = 0.3175 \mu\text{m}$. The long-time potential amplitude, V_∞ , and the lattice spacing d are indicated in the graphs. The dimensionless parameter ν (see equation (5)) takes the values (0.0905, 0.2350, 0.2036, 0.1018) for graphs (a)–(d). The setups (a) and (b) are designed to have the same band bottom. The simulations are run until a time $4 \times 10^4 t_0 = 5.5 \text{ s}$. Note that the scale of $\sigma(t)$ is considerably enlarged. The initial value, $\sigma(0)$ (only observed with some magnification), is spurious, and is related to the discrete approximation to the derivatives in equation (6).

is exponentially small, corresponding to an atom transmission probability, $T(L_{\text{lat}}) \propto \exp(-\kappa L_{\text{lat}})$, where $\kappa \propto \sqrt{E_{\text{min}} - \mu}$, with E_{min} being the bottom of the conducting band. This situation whereby one soon reaches the regime $\mu < E_{\text{min}}$, is not interesting for our purposes because we need some appreciable flux to form a useful black-hole configuration. In particular, we are typically interested in considering condensates so large that the time needed to reach the bottom of the conduction band is longer than the typical lifetime of the condensate.

A further argument can be invoked in favor of wide bands. In virtually all the cases we have addressed, $\text{Re } \bar{\mu}(t)$ drops until it almost reaches the bottom of the conduction band, where leaking is slow. In the resulting regime, the density in the lattice is very small, $g\bar{n}_r \ll \hbar^2 k_L^2/m$, where \bar{n}_r is the mean density in the optical lattice, as defined precisely in subsection 4.2. We show in appendix C that, in this regime of low interactions, the width of the conduction band for the linear perturbations (whose evolution is governed by the BdG equations) is very close to that obtained for the linear Schrödinger equation, and the corrections are computed there. This means that the optical lattice acts like a low-pass filter, the band width being the equivalent of

the cutoff frequency. The higher the cutoff, the wider the transmission band of the lattice is. As a consequence, fluctuations on the subsonic side are transmitted away through the optical lattice, which reduces the space fluctuations in the chemical potential.

Another trend can be observed in the second row of figure 2. When placing μ_0 slightly below the top of the conduction band or in the first gap, as figure 2(d) illustrates, leaking occurs faster, but the reached regime presents much larger fluctuations than in the other cases shown in figure 2. For the purpose of keeping $\sigma(t) \ll 1$, a more favorable situation for the chemical potential is shown in figure 2(c). There, for the same length, d , as in figure 2(d) but a higher barrier amplitude, V_∞ , the chemical potential is initially placed in the final conduction band. This case clearly yields smaller fluctuations, even though the width of the conduction band is smaller. This shows that, besides having wide bands, one also needs μ_0 to be placed close to the bottom of the final conduction band in order to obtain a more favorable quasi-stationary regime. This point is further discussed in the next subsection (4.2).

Within the nearly free particle approximation ($v \ll 1$), the bottom and top of the first conduction band are given by the relations:

$$\begin{aligned} E_{\min}(v) &= 8E_R \left(v - v^2 + O(v^4) \right) \\ E_{\max}(v) &= E_R \left(1 + 4v - 2v^2 + O(v^4) \right), \end{aligned} \quad (11)$$

where $E_R \equiv \hbar^2 k_L^2 / 2m$ is the recoil energy of the optical lattice. Given that $k_L = \pi/d$, the condition that the initial chemical potential lies within the final conduction band, that is,

$$E_{\min}(v) < \mu_0 < E_{\max}(v), \quad (12)$$

is guaranteed to be satisfied if

$$8E_R v < \mu_0 < E_R. \quad (13)$$

The left inequality is just

$$\frac{V_\infty}{2} < \mu_0, \quad (14)$$

while the right inequality can be rewritten as:

$$d < \frac{\pi}{\sqrt{2}} \xi_0. \quad (15)$$

Equations (14) and (15) express a sufficient condition to satisfy equation (12).

4.1.2. Non adiabatic effects. In the favorable situation shown in figure 2(a), the dependence on τ is not important as long as $\tau \gg t_0$. A simulation is presented in figure 3, showing that in the fast regime ($\tau \sim t_0$), and due to the high-frequency excitations induced by the short lowering time scale, $\sigma(t)$ remains higher than in the adiabatic case (see figure 2(a)).

4.2. Quasi-stationary regime

From the discussion in the previous subsection (4.1), and particularly through the situation shown in figure 2(a), we have learned that, for wide enough bands, initial chemical potential close to the bottom of the final conduction band, adiabatic evolution ($\tau \gg t_0$), and a typical

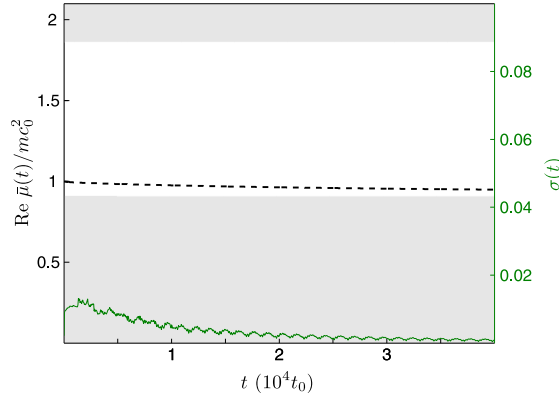


Figure 3. Fast barrier lowering. Same parameters as in figure 2(a) except for $\tau = t_0$, which is too short a time to be observed on this scale.

setup, the system evolves towards a quasi-stationary regime in a time frame that is shorter than the lifetime of a condensate.

The quasi-stationary regime can be defined as a regime where $\text{Re } \mu(x, t)$ is essentially uniform [$\sigma(t) \ll 1$] and whose global time variations take place on a time scale of the order of, or greater than, the condensate lifetime. We focus our study on the most favorable quasi-stationary scenarios, which we identify here with those satisfying $\sigma(t) \lesssim 10^{-4}$.

The achievement of this regime is of general interest as a scenario for the study of atom quantum transport. In particular, one may expect spontaneous Hawking radiation to be detectable above a quasi-stationary background with small spatial fluctuations.

In this section, we discuss several features of the condensate wave function for the quasi-stationary regime. For illustration purposes, all the graphs considered in this subsection have been obtained for a system with the parameters found in figure 2(a), which are sufficiently representative.

By writing the condensate wave function as $\Psi(x, t) = \sqrt{\rho(x, t)} e^{i\phi(x, t)}$, we may introduce two local velocities:

$$\begin{aligned} v(x, t) &\equiv \frac{\hbar \partial_x \phi(x, t)}{m}, \\ c(x, t) &\equiv \sqrt{\frac{g\rho(x, t)}{m}}, \end{aligned} \quad (16)$$

with $v(x, t)$ being the local condensate flow velocity and $c(x, t)$ being the local speed of sound. The spatial variations of both velocities are small in the subsonic and supersonic regions, but not in the lattice. We note that, in that region, $c(x, t)$ must not be regarded as the lattice sound speed (see appendices B and C).

The profile of both quantities computed at a time, $t = 4 \times 10^4 t_0$, after a barrier removal time of $\tau = 500 t_0$, is shown in figure 4. The subsonic zone shows an essentially flat (uniform) density and flow speed profile, in the sense that the spatial fluctuations are on the order of $\sim 10^{-4} n_0$ for the density and $\sim 10^{-3} c_0$ for the flow speed, which is too small to be observed in figure 4. An approximate analytical formula (equation (A.21)) for the wave function of the

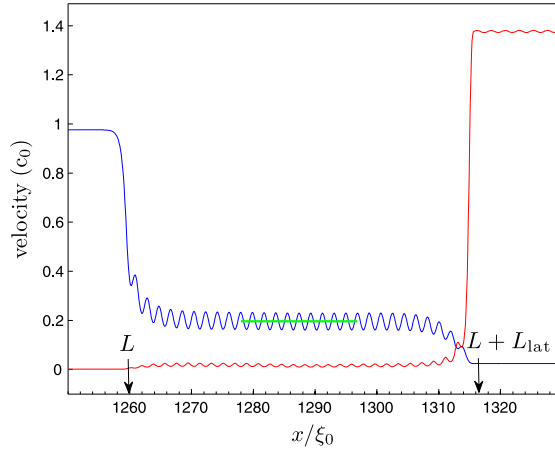


Figure 4. Local flow velocity (red) and local speed of sound (blue) at a late time, $t = 4 \times 10^4 t_0$. The horizontal green segment shows the speed of sound in the optical lattice, computed using (C.15), with the coefficients there appearing to be computed numerically. Within this finite lattice, the mean density is $\bar{n}_r(t)$, computed by dropping 10 lattice sites at each end of the lattice. System parameters are the same as in figure 2(a).

initially confined condensate fits the numerical results within this level of accuracy. This good agreement reflects the low value of the flow velocity in the condensate region.

On the other hand, in the deep central region of the optical lattice, Bloch's theorem is satisfied. We introduce the space-averaged density, $\bar{n}_r(t)$, by averaging $\rho(x, t)$ over the optical lattice after excluding 10 lattice sites at each end of the lattice. That average density, combined with numerically computed quantities that depend on the optical lattice potential, yields an effective sound velocity (see equation (C.15)) that is plotted as a horizontal green segment spanning the averaged region in figure 4. One can clearly see that, within the optical lattice, the flow is subsonic, with the horizon lying on its right edge. In the quasi-stationary regime, $\bar{n}_r(t)$ decreases at a rate comparable to the inverse lifetime of the condensate, as the inset in figure 5 shows.

At the edges of the lattice, there are strong variations of the density due to the the matching between the vastly different densities found on both the subsonic and the supersonic sides.

A check on the approximate validity of Bloch's theorem in the presence of nonlinear corrections, for the central part of the optical lattice and in the quasi-stationary regime, is also shown in figure 5. In this graph, the real part of $\bar{\mu}(t)$ is compared with the time-dependent chemical potential computed using $\bar{n}_r(t)$ and assuming zero Bloch momentum, as explained in the first paragraphs of appendix B. The good agreement between the two curves suggests that the condensate flows with a very small Bloch momentum.

In the supersonic zone, once in the quasi-stationary regime, both density and flow-speed profiles are almost uniform. This is hinted at in figure 4, but is not shown explicitly. Part of the nonflat behavior is due to small spurious reflections; see appendix D for details. Conservation of the chemical potential and the near absence of interaction effects in this zone make the flow speed almost uniform, because the chemical potential is almost fully transformed into kinetic energy. On the other hand, the supersonic density decays with time as the reservoir is depleted, but the process is such that, at each instant, the density profile remains essentially uniform (not

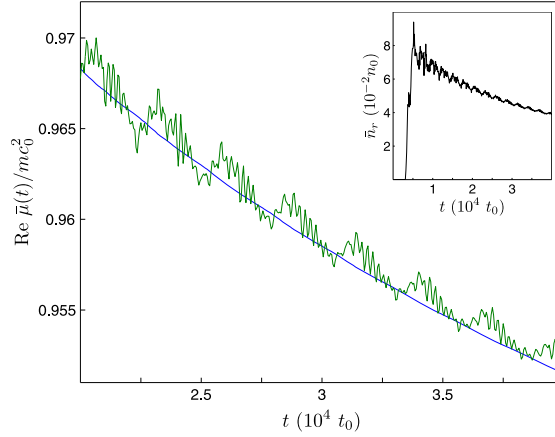


Figure 5. The same system parameters as in figure 2(a). Blue: real part of the space-averaged chemical potential, $\bar{\mu}(t)$ (see equation (8)). Green: chemical potential for zero Bloch momentum computed from the results of appendix C and using $\bar{n}_r(t)$ as the mean density, which is precisely defined in the previous figure and plotted in the inset.

shown). An inhomogeneous density profile would show up only on a space scale much larger than that used in this simulation. A comparison of the decaying supersonic density, $n_d(t)$, and the nearly constant supersonic side speed, $v_d(t)$, is shown in figure 6 (subindex d stands for ‘downstream’ region). The emission rate per particle (not shown), as computed from equation (10), is practically identical to the product $n_d(t)v_d(t)$, except for a numerical factor corresponding to the instantaneous total number of particles, which in the quasi-stationary regime is practically constant. This emission rate gives us the typical time scale for the variation of the number of particles of the system, which is approximately the time scale for the variation of μ . In the quasi-stationary regime considered here, it is $\sim 10^{-6} - 10^{-7} t_0^{-1}$, from which we infer that the typical variation time of the chemical potential is $\sim 10^6 - 10^7 t_0$, much longer than the lifetime of a condensate, which is $\sim 10^4 t_0$.

We conclude that the realization of this quasi-stationary regime needs two fundamental ingredients: the existence of a band structure and the presence of interactions. Without a band structure such as the one provided by the optical lattice, the condensate would continue leaking through the barrier at a fast rate. On the other hand, the presence of interactions (as reflected in the fact that $\partial\mu/\partial n \neq 0$) allows the condensate to stabilize its flow near the bottom of the conduction band. If the interactions in the subsonic region were negligible, the condensate would empty quickly (if μ_0 lay in the final conducting band) or it would remain confined (if μ_0 lay in the final gap).

Such trends can be seen in the accompanying videos (available at stacks.iop.org/njp/16/123033/mmedia) that represent simulations for the same parameters as in figure 2(a) except for $L = 10 \mu\text{m}$ and $N = 250$. The qualitative conclusions are similar. In video 1, we see the time evolution of the density of a condensate confined by an ideal optical lattice of 30 barriers. We see that the system achieves the desired quasi-stationary regime. On the other hand, in video 2, we introduce a similar potential, but with a single barrier. We observe that the fluid leaks faster through the single barrier because there is no structure providing a conduction band whose lower boundary is raised close to the chemical potential in order to efficiently slow down the

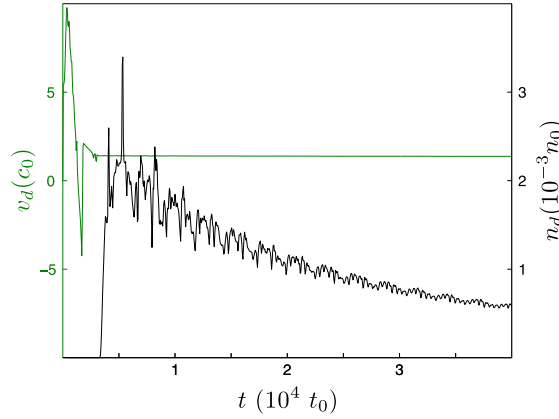


Figure 6. Time evolution of the mean density and the mean flow velocity on the supersonic side. The means are taken over the entire downstream region. System parameters are the same as in figure 2(a).

density decrease. This conclusion applies to the class of setups we are considering, which include an initially confined condensate. In other approaches, such as that of [21], the condensate is projected onto a potential barrier and a quasi-stationary black-hole regime is also eventually reached.

The interaction plays the additional role of providing relaxation channels, whereby the condensate lowers its energy while some collective modes are excited. The existence of Landau instabilities (see appendix B) when μ_0 lies well above E_{\min} can be clearly observed in the upper right corner of figure 5 of [41], whose chosen parameters are similar to those of the present work. The low value of the critical velocity helps us understand the small value of the condensate Bloch momentum, which we infer from the numerical results shown figure 5 of this article. The appearance of instabilities can also be viewed as responsible for the fast lowering of the chemical potential after being initially prepared above the final conduction band, as shown in figure 2(d). This interpretation is consistent with the relatively large values found for $\sigma(t)$ when μ_0 is considerably above E_{\min} .

5. Gaussian-shaped optical lattice

Here we perform the same analysis as in the previous section, but we use a more realistic optical lattice that includes a Gaussian envelope [38, 42, 43]:

$$V(x, t) = V(t) \cos^2[k_L(x - L)] \exp\left[-2\left(\frac{x - L}{\tilde{w}}\right)^2\right] \quad (17)$$

where $\tilde{w} = w/\cos(\theta/2)$ (with w being the laser beam width and θ being the angle between the laser beams) plays the role of an effective lattice length. The time dependence of $V(t)$ is the same as in equation (4). Usually, \tilde{w} varies in a range of 10–200 μm . Here, L is the position of the maximum of the lattice Gaussian envelope. For consistency, we replace the hard wall at $x = 0$ with a Gaussian barrier of the type $V_L(x) = U \exp(-2x^2/w_L^2)$ with $w_L = 2 \mu\text{m}$ and $U \gg \mu_0$ in order to simulate a more realistic confinement on the left side. This time-independent potential

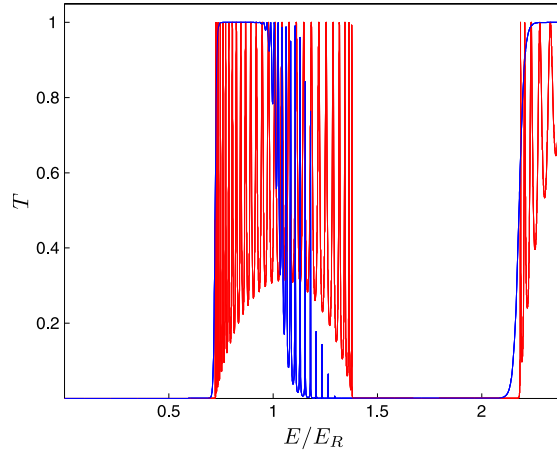


Figure 7. Single atom transmission probability $T(E)$, as a function of energy, for a realistic (Gaussian-shaped) optical lattice (blue) with the instantaneous value $V(t) = 1.6E_R$ (see equation (17)) and $\tilde{w} = 30d$, with E_R defined after equation (11), and for an ideal (flat) optical lattice (red) with same amplitude, $V(t)$, and $n_{\text{osc}} = 30$.

must be added to the time-dependent potential (17), which provides confinement on the right; see appendix A for a detailed description of the initial confinement.

In the ‘adiabatic’ regime ($\tilde{w} \gg d$), the solutions of the linear Schrödinger equation for this type of potential can show features similar to those found for an ideal optical lattice with the same instantaneous amplitude, $V(t)$, as one can see in figure 7, where the transmission bands are compared. If we focus on the long-time limit ($V(t) = V_\infty$), the realistic potential acquires the form

$$V(x) = V_\infty(x) \cos^2[k_L(x - L)], \quad (18)$$

where

$$V_\infty(x) = V_\infty \exp\left[-2\left(\frac{x - L}{\tilde{w}}\right)^2\right] \quad (19)$$

is a slowly varying function. Then, we have a locally ideal optical lattice at each point of the space with amplitude $V_\infty(x)$. Bloch’s theorem can also be applied locally, resulting in a local band structure that is plotted as a function of space in figure 8. A similar type of reasoning was already used in [44–46]. The left panel presents the setup whose single atom transmission is plotted in figure 7. Since the bottom of the lowest lattice conduction band is an increasing function of the periodic potential amplitude, the bottleneck for transmission across the realistic lattice occurs at the center of its Gaussian envelope. This fact explains the accurate coincidence between the bottom of both conduction bands shown in figure 7. We also see that for $E > E_R$, which is defined after equation (11), the particle encounters a gap somewhere along the Gaussian lattice, and this explains why the transmission begins to decay for $E > E_R$ in figure 7. For $E_{\text{min}}(v) < E < E_R$, the setup shows a plateau of essentially perfect atom transmission. The absence of interference oscillations in this region is due to the adiabatic variation of the lattice envelope. The right panel presents the different case of $E_R < E_{\text{min}}(v)$. From the preceding

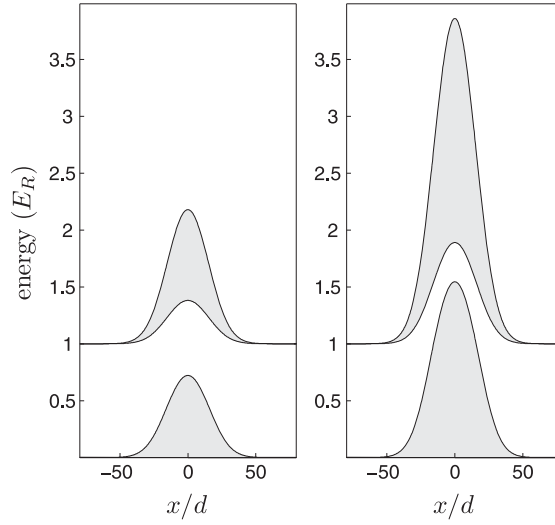


Figure 8. Plot of the spatially dependent energy bands for a realistic optical lattice with $\tilde{w} = 30d$. We use the same color criterion as we did for the band structure of figure 2. Left panel: the instantaneous value of the amplitude is $V(t) = 1.6E_R$, which corresponds to the case of figure 7. Right panel: the instantaneous value of the amplitude is $V(t) = 4E_R$. In this case, the first conduction band becomes ineffective, as we can expect from the plot, since transmission is always hindered somewhere for the energies of interest.

arguments, we do not expect to find a conduction band that can be numerically confirmed. We conclude that, in order to have a well-defined conduction band for the realistic lattice, the condition $E_R > E_{\min}(\nu)$ is required, which implies $V_\infty < 2.33 E_R$. Combining all these considerations, we conclude that a necessary condition for achieving a quasi-stationary regime is $E_{\min}(\nu) < \mu_0$. We also require $\mu_0 < E_R$ to avoid having μ_0 lying too high above $E_{\min}(\nu)$, which, as found for the ideal lattice, tends to generate relatively high values of $\sigma(t)$. This last inequality is equivalent to equation (15).

Here, space can also be divided into three zones. In the quasi-stationary regime, both the subsonic and supersonic zones are located where the Gaussian envelope amplitude is negligible compared to the chemical potential, that is, where

$$V_\infty(x) \ll \text{Re } \bar{\mu}(t) \quad (20)$$

as seen in equations (8) and (19). For the subsonic side to be well differentiated, we set $L \gg \tilde{w}$. The optical lattice region is the complementary of the subsonic and supersonic zones (i.e., the region where (20) does not apply).

The requirements of quasi-stationarity are similar to those formulated for the ideal optical lattice. Specifically, the quasi-stationary regime requires broad conduction bands, an initial chemical potential close to the bottom of the final conduction band, and a barrier amplitude that does not evolve very fast. We also find that the condensate leaks relatively fast until $\text{Re } \bar{\mu}(t)$ (equation (8)) approaches the bottom of the conduction band. All these features can be observed in figure 9, which is the Gaussian-envelope equivalent of figures 2 and 3. We reach a quasi-stationary state in which $\sigma(t) \sim 10^{-4}$. The bands in figure 9 are computed as in the ideal case,

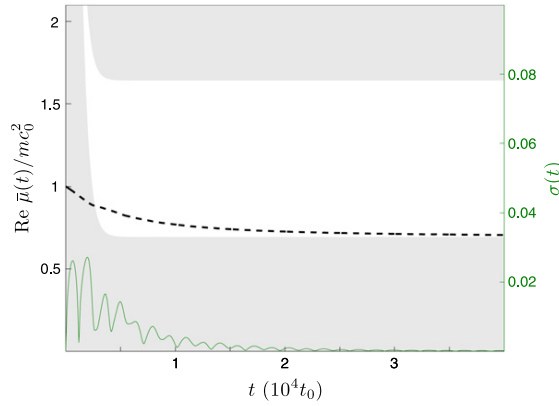


Figure 9. Time evolution of the real part of the chemical potential and its fluctuation spread in a realistic (Gaussian-shaped) optical lattice. The parameters are $\tilde{w} = 50 \mu\text{m}$, $d = 600 \text{ nm}$, $\tau = 500 t_0$, and $V_\infty = 1.5 mc_0^2$ and we have taken $\xi_0 = 0.3053 \mu\text{m}$. The confinement parameters are $N = 9161$, $L = 420 \mu\text{m}$, and $\omega_{\text{tr}} = 2\pi \times 4 \text{ kHz}$.

assuming a uniform barrier amplitude, $V(t)$. As noted in the discussion of figure 7, the positions of the bottom of the ideal and the realistic conduction (or transmission) bands are very similar, so the lower threshold of the transmission band can still be a good reference value to discuss the evolution of $\bar{\mu}(t)$.

We notice that in the Gaussian case, the condensate apparently leaks from the beginning of the simulation. What is actually happening is that the chemical potential is already lowered by the initial expansion of the condensate towards the neighboring, low-amplitude region of the Gaussian optical lattice, even when the leaking (towards the right side of the Gaussian envelope) is not yet occurring. This process can be observed in the simulation later presented in video 3 at the end of section 5.1. The situation contrasts with that shown in figure 2, where the condensate only begins to leak when the chemical potential is placed within the conduction band.

We also study the corresponding quasi-stationary state. For that purpose, we take a snapshot of the configuration at $t = 4 \times 10^4 t_0$ for the parameters in figure 9. We compare the profiles of $c(x, t)$ and $v(x, t)$ in figure 10, which is the realistic equivalent of figure 4. The apparently sharper oscillations, as compared to those in figure 4, are due to the different horizontal scales used. The larger oscillations of the flow velocity beyond the horizon with respect to those inside the lattice subsonic region in figure 4 can be explained because of the large difference in the space-averaged flow velocities. In the supersonic region, we again find essentially flat profiles for the density and flow velocities, with their time evolution shown in figure 11. The general features of this quasi-stationary configuration are similar to those of the ideal case, but some interesting new features appear.

5.1. Location of the sonic horizon and related properties

We notice in figure 10 that the horizon seems to be placed at the maximum of the Gaussian envelope. This can be explained on general grounds by invoking the properties of the quasi-stationary regime and the adiabaticity condition, $\tilde{w} \gg d$, which allows us to think in terms of a

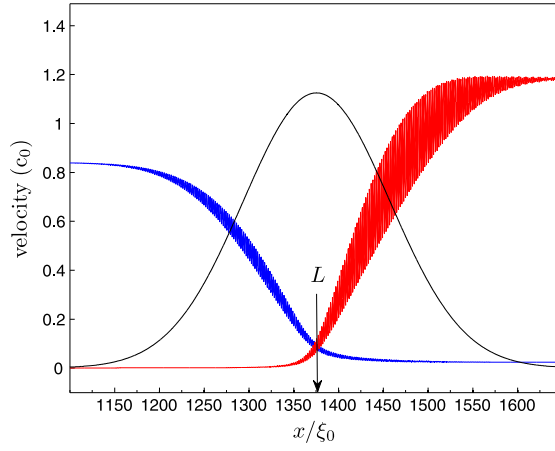


Figure 10. Local flow velocity (red) and local speed of sound (blue) at $t = 4 \times 10^4 t_0$. System parameters are the same as in figure 9.

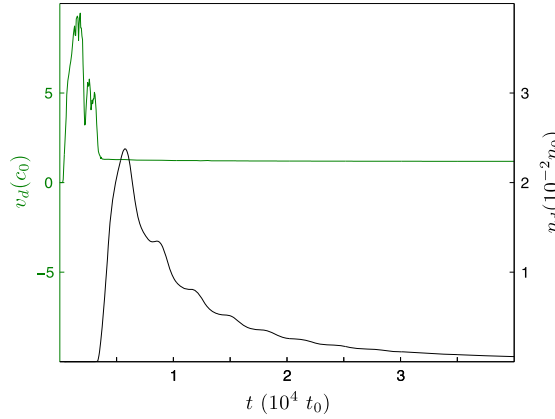


Figure 11. Time evolution of the mean density and the mean flow velocity on the supersonic side for a condensate emitting through a Gaussian-shaped optical lattice. System parameters are the same as in figure 9.

local band structure stemming from a periodic potential of local amplitude $V_\infty(x)$. Then we can use an adiabatically space-dependent version of equations (C.10)–(C.18) (where the sound speed, atom current, and chemical potential are obtained for an infinite optical lattice) by making every parameter slowly dependent on x .

In particular, we take:

$$\begin{aligned}
 s(x) &= \left[\frac{gn_r(x)}{m^*(x)} \alpha_0^{(1)}(x) \right]^{\frac{1}{2}} \\
 j(x) &\simeq n_r(x) \bar{v}(x) \\
 \mu(x) &\simeq E_{\min}(x) + \frac{1}{2} m^*(x) \bar{v}^2(x) + m^*(x) s^2(x),
 \end{aligned} \tag{21}$$

where we neglect the time dependence because the system is assumed to already be in the quasi-stationary regime. The local averages for n_r , \bar{v} are taken over several lattice periods. In the quasi-stationary regime, the chemical potential is already close to the bottom of the conduction band, so the perturbative study used in appendix C is valid. Taking spatial derivatives, while noting that the chemical potential is almost uniform, $\mu(x) \simeq \bar{\mu}$, and that $\partial_x j(x)$ can be neglected (as implied by the continuity equation and quasi-stationarity), we arrive at:

$$0 = E'_{\min} + \frac{1}{2}m^{*\prime}\bar{v}^2 + \frac{\alpha_0^{(1)\prime}}{\alpha_0^{(1)}}m^*s^2 + m^*(\bar{v}^2 - s^2)\frac{\bar{v}'}{\bar{v}}. \quad (22)$$

The quantities $E_{\min}(x)$, $m^*(x)$, $\alpha_0^{(1)}(x)$ depend on x through the amplitude of the envelope, $V_\infty(x)$, and they increase with its value, provided that the envelope amplitude is always positive (see equation (C.16)). Therefore, the first three terms in the right-hand side of (22) have the same sign.

Let us assume that we have a horizon ($s = \bar{v}$) somewhere in the optical lattice. We prove next that a necessary implication is that an envelope maximum or minimum exists at that point. It has just been noted that the first three terms in (22) have the same sign. Thus, their sum can only be zero whenever the derivative of the amplitude is zero (i.e., when $V'_\infty(x) = 0$). In our setup, this means that we have an amplitude maximum at the horizon.

Now we consider the inverse implication. Assume we have $V'_\infty(x) = 0$, which in our setup is the case at $x = L$. This implies that the first three terms in (22) are zero. As a consequence, we are left with two possibilities:

$$s(L) = \bar{v}(L) \quad (23)$$

(i.e., a horizon) or $\bar{v}' = 0$. By the continuity equation, the second option implies a density minimum, which must be ruled out in our current single-Gaussian-barrier setup. However, it can be a perfectly feasible result in other experimental contexts.

Finally, we note equation (22) can also be written as

$$0 = E'_{\min} + \frac{1}{2}m^{*\prime}(\bar{v}^2 + 2s^2) + m^*(\bar{v}\bar{v}' + 2ss'), \quad (24)$$

and, as a corollary of the foregoing analysis, we find that at the horizon, $s'(L) = -\bar{v}'(L)/2$.

We can further exploit the previous results. For example, we can obtain the value of the density and the current at $x = L$ as a function of $\bar{\mu}$:

$$gn(L) = \frac{2}{3} \frac{\bar{\mu} - E_{\min}}{\alpha_0^{(1)}},$$

$$j(L) = n_r(L)\bar{v}(L) = \left(\frac{2}{3}\right)^{\frac{3}{2}} \frac{(\bar{\mu} - E_{\min})^{\frac{3}{2}}}{g\alpha_0^{(1)}\sqrt{m^*}}, \quad (25)$$

which are very good approximations to the actual numerical values. Here, the dependence of the various parameters on L is understood. Using (25), we can arrive at a differential equation for the time evolution of $\bar{\mu}$. First, we note that from the continuity equation, we can write:

$$\frac{dN_L}{dt} = -j(L), \quad (26)$$

where N_L is the number of particles contained between $x = 0$ and $x = L$. As the subsonic region is in the Thomas-Fermi regime (see appendix A), we can take $\bar{\mu} \simeq gN_{\text{sb}}/L_{\text{sb}}$, where N_{sb} is the number of particles in the subsonic region and L_{sb} is its size. Since the density in the optical lattice is small, we can assume $N_L \simeq N_{\text{sb}}$ (which implies $\bar{\mu} \propto N_L$), and write equation (26) as:

$$\frac{d\bar{\mu}}{dt} = -C(\bar{\mu} - E_{\text{min}})^{\frac{3}{2}}, \quad (27)$$

where C is a positive constant independent of $\bar{\mu}$. The solution of this equation is

$$\bar{\mu}(t) = E_{\text{min}} + \frac{4}{C^2(t - t_1)^2}, \quad (28)$$

(with t_1 an integration constant), which fits the numerical data of figure 9 reasonably well.

Finally, we can estimate the value of the Hawking temperature, which is given by:

$$k_B T_H = \frac{\hbar}{2\pi} \frac{d}{dx} [\bar{v}(x) - s(x)]_{x=L} \quad (29)$$

If we note that we operate in the nearly-free atom approximation ($v \ll 1$) and in the weak interaction regime ($gn_r \ll E_R$), and derive twice the third equation (21), we obtain

$$k_B T_H \simeq \frac{\hbar}{2\pi\tilde{w}} \sqrt{\frac{3V_\infty}{m^*}} (1 - v), \quad (30)$$

which gives a good estimate of the numerical value of the Hawking temperature. Noting that $V_\infty \sim \mu_0$, $m^* \sim m$, we obtain $k_B T_H \sim \xi_0 \mu_0 / \tilde{w} \sim 10^{-2} \mu_0 \ll \mu_0$. The temperature of the condensate is typically of the order of μ_0/k_B , so we conclude that $T_H \sim 10^{-2} T \ll T$.

To observe the birth of the black hole and to check that the horizon position naturally evolves towards the maximum of the optical lattice envelope, we have created a movie (video 3) that shows the time evolution of the coarse-grained velocities (\bar{c} , \bar{v}) of the emitting condensate, using the setup parameters of figure 9. At long times, the predicted coincidence between the sonic horizon and the maximum of the Gaussian envelope in the stationary regime can be clearly observed.

When applied to an ideal optical lattice, the above arguments on the position of the horizon yield no preferred point for the location of the horizon because the envelope is uniform. Actually, in the bulk of the lattice, since $V'_\infty = 0$ everywhere, the natural outcome (from the discussion leading to equation (23)) is $\bar{v}' = 0$ everywhere (i.e., the mean velocity and, by quasi-stationarity, the mean density are also uniform, as can be observed in figure 4). This fact only leaves two options: either the lattice bulk is subsonic or it is supersonic. The latter choice is energetically unstable (see [41]) and as a consequence, the subsonic regime is energetically favored in the bulk of the lattice. In the rightmost region, where the potential is not present, the flow must be supersonic, so the only possibility for the horizon is to lie at the right extreme of the lattice, as one can see in figure 4.

6. Conclusions

Within a mean-field description, we have investigated the process where an initially confined atom condensate is coherently outcoupled as the barrier on one side is gradually lowered. The

goal has been to identify the barrier-lowering protocol that best leads to a quasi-stationary sonic black hole located at the interface between subsonic and supersonic flow. We find that the use of an optical lattice for the lowered barrier is convenient for achieving a regime of quasi-stationary flow with minimal value of the fluctuation spread. First, we focused on an optical lattice of finite length and uniform amplitude. We found that the long-time band structure of the optical lattice greatly influences the asymptotic behavior of the emitted atom flow. Within this class of setups, the best quasi-stationary flow was achieved when the lowest conduction band was broad and the initial chemical potential lay not much higher than the bottom of the final conduction band. In optimal cases, the relative value of the spatial fluctuations can be as small as $\sigma(t) \sim 10^{-4}$. When we replaced the uniform amplitude of the optical lattice by a more realistic Gaussian envelope, we found that the results are similar to those of a uniform lattice with the amplitude of the envelope maximum. Quite interestingly, we argued analytically and checked numerically that, in the quasi-stationary regime, the horizon separating the regions of subsonic and supersonic flow was pinned down right at the Gaussian maximum. We also found that the Gaussian envelope was quite efficient in guaranteeing a small deviation from the ideal stationary flow.

Whether the quasi-stationary regimes identified in this article can become scenarios for the detection of Hawking radiation is something that will have to be confirmed by a future study of the quasiparticle dynamics operating against the background of seemingly favorable mean-field configurations.

Acknowledgments

We thank I Carusotto and R Parentani for valuable discussions. This work has been supported by MINECO (Spain) through grants FIS2010-21372 and FIS2013-41716-P, Comunidad de Madrid through grant MICROSERES-CM (S2009/TIC-1476), and the Institut Universitaire de France.

Appendix A. Initial configuration of the condensate

In this appendix, we compute the initial profile of the condensate, which at early times ($t < 0$) experiences a confining time-independent potential. We require a hard-wall boundary condition at $x = 0$, which implies, via continuity equation, that the phase of the condensate is constant in space. The amplitude $A(x) \equiv |\Psi(x)|$ of the solution to the time-independent GP equation (3), in the region where there is no potential, satisfies the equation

$$\left(-\frac{\hbar^2}{2m} \partial_x^2 + gA^2 \right) A = \mu_0 A. \quad (\text{A.1})$$

As is well known, this equation can be interpreted as the equation of motion for a particle with ‘coordinate’ A and ‘time’ x in a certain potential

$$W(A) = \tilde{\mu}_0 A^2 - \frac{\tilde{g}}{2} A^4$$

$$\tilde{\mu}_0 = \frac{m}{\hbar^2} \mu_0, \quad \tilde{g} = \frac{m}{\hbar^2} g. \quad (\text{A.2})$$

Invoking ‘energy’ conservation, the equation can be integrated as

$$\frac{1}{2}A'^2 + W(A) = E_A, \quad (\text{A.3})$$

where E_A is the total energy of this effective motion.

Following [15], equation (A.3) can be rewritten in terms of $\rho(x) = A^2(x)$ as

$$\rho'^2 = 4\tilde{g}(\rho - e_1)(e_2 - \rho)(e_3 - \rho), \quad (\text{A.4})$$

where

$$0 = e_1 \leq \rho \leq e_2 < e_3, \quad (\text{A.5})$$

and $e_{2,3}$ are the zeros of

$$\rho^2 - 2\frac{\tilde{\mu}_0}{\tilde{g}}\rho + 2\frac{E_A}{\tilde{g}} = 0. \quad (\text{A.6})$$

The solution can be expressed in terms of elliptic functions [40]. Imposing the boundary condition $\rho(0) = 0$, one obtains a solution of the form

$$\rho(x) = e_2 \operatorname{sn}^2(\sqrt{\tilde{g}e_3}x, \nu), \quad \nu = \frac{e_2}{e_3}. \quad (\text{A.7})$$

In order to determine $e_{2,3}$, another boundary condition is needed, together with the particle number normalization $\int dx \rho(x) = N$. From (A.2) and (A.6), the chemical potential can be written as

$$\mu_0 = g \frac{e_2 + e_3}{2}. \quad (\text{A.8})$$

A.1. Ideal confinement

The ideal confinement boundary condition is defined as $A(L) = 0$, and the condensate is confined between 0 and L . Using equation (A.7), we find

$$\sqrt{\tilde{g}e_3}L = 2nK(\nu), \quad n \in \mathbb{N}, \quad (\text{A.9})$$

where $K(\nu)$ is the complete elliptic integral of the first kind [47].

Hereafter, we work with the ground state ($n = 1$). The particle number normalization is

$$N = \int_0^L dx e_2 \operatorname{sn}^2(\sqrt{\tilde{g}e_3}x, \nu). \quad (\text{A.10})$$

By performing the integral in equation (A.10) and using (A.9), we have

$$N = \frac{e_2}{\sqrt{\tilde{g}e_3}} \frac{2}{\nu} [K(\nu) - E(\nu)], \quad (\text{A.11})$$

where $E(\nu)$ is the complete elliptic integral of the second kind [47]. Equations (A.9) and (A.11) lead to

$$N\tilde{g}L = 4K(\nu)[K(\nu) - E(\nu)], \quad (\text{A.12})$$

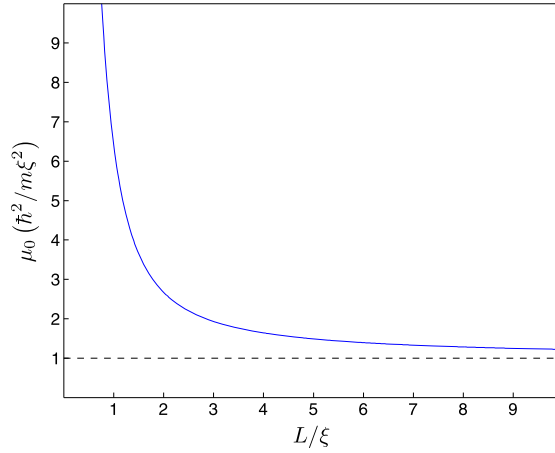


Figure 12. Computation of the chemical potential as a function of L/ξ using equations (A.13) and (A.15) for an ideal lattice confined between hard walls and in equilibrium. When $L/\xi \ll 1$, we are in the Schrödinger limit in which $\mu_0 \sim 1/L^2$, and when $L/\xi \gg 1$, we are in the Thomas–Fermi regime, and then $\mu_0 \simeq \hbar^2/m\xi^2$.

or

$$4K(\nu)[K(\nu) - E(\nu)] = \left(\frac{L}{\xi}\right)^2, \quad (\text{A.13})$$

where the healing length, $\xi \equiv \sqrt{\hbar^2 L/mgN}$, is not identical to ξ_0 as defined in section 2.

After eventually solving for ν , e_2 , and e_3 , equation (A.7) can be rewritten as

$$A(x) = \sqrt{e_2} \operatorname{sn}\left(2K(\nu)\frac{x}{L}, \nu\right). \quad (\text{A.14})$$

For the chemical potential, using (A.8) and (A.9), we obtain

$$\mu_0 = \frac{2\hbar^2}{mL^2}(1 + \nu)[K(\nu)]^2. \quad (\text{A.15})$$

Taking into account that ν is a function of L/ξ , as given by equation (A.13), we plot equation (A.15) in figure 12. In order to find ν , equation (A.13) must be solved numerically. However, good approximate solutions can be found. We can clearly distinguish two different regimes: $L \ll \xi$ and $L \gg \xi$. The physical interpretation is straightforward because the ratio between the kinetic energy and the interaction energy is

$$\frac{E_{\text{int}}}{E_{\text{kin}}} \sim \frac{gN/L}{\hbar^2/mL^2} \sim \frac{\hbar^2/m\xi^2}{\hbar^2/mL^2} = \left(\frac{L}{\xi}\right)^2. \quad (\text{A.16})$$

Then, $L \ll \xi$ is the Schrödinger limit, in which we have $\nu \simeq 0$. In that limit, we arrive at the well-known results: $\sqrt{ge_3}L = \pi$ and $\rho(x) = e_2 \sin^2(\pi x/L)$. In all the cases considered in this work, $L \gg \xi$, so we work in the limit in which interactions represent the main contribution to the chemical potential (Thomas-Fermi regime). $K(\nu)$ diverges when $\nu \rightarrow 1$, while $E(\nu)$ remains finite. From (A.13), this means that $\nu \simeq 1$. In fact, there are cases in which $1 - \nu$ is so small that it falls below computer floating-point relative accuracy. In those cases, the only way to obtain

the solution is through asymptotic expansion. One can prove that, in that limit [47],

$$K(\nu) \simeq \ln \frac{4}{\sqrt{1-\nu}}, \quad E(\nu) \simeq 1. \quad (\text{A.17})$$

Thus, equation (A.13) is rewritten as

$$K^2 - K - \frac{r^2}{4} = 0, \quad r = \frac{L}{\xi}, \quad (\text{A.18})$$

and from its solution we get $2K = 1 + \sqrt{1+r^2}$. Therefore, $1 - \nu = 16e^{-2K} \ll 1$, which implies both $e_2 \simeq e_3$ and $\mu_0 \simeq ge_2$. Equation (A.9) implies

$$e_3 = \frac{4K^2 N}{r^2 L} \simeq \left(1 + 2\frac{\xi}{L}\right) \frac{N}{L}, \quad (\text{A.19})$$

and then

$$\frac{\mu_0}{\hbar^2/m\xi^2} = \frac{n_0}{N/L} = \left(\frac{\xi}{\xi_0}\right)^2 = 2(1 + \nu) \left[\frac{K(\nu)}{r}\right]^2 \simeq 1 + 2\frac{\xi}{L} + 2\left(\frac{\xi}{L}\right)^2. \quad (\text{A.20})$$

Collecting all these results, the wave function can be effectively approximated by

$$\Psi_0(x) \equiv \begin{cases} \sqrt{e_2} \tanh\left(2K\frac{x}{L}\right), & 0 \leq x \leq \frac{L}{2} \\ \sqrt{e_2} \tanh\left[2K\left(1 - \frac{x}{L}\right)\right], & \frac{L}{2} \leq x \leq L \end{cases} \quad (\text{A.21})$$

because $\text{sn}(x, 1) = \tanh(x)$. The function \tanh quickly reaches the asymptotic value 1, which means that in the central zone of the confinement region, the solution is essentially flat.

A.2. Ideal optical lattice potential

For computational purposes, the initial rightmost boundary condition is also taken as $A(L) = 0$, but now half a period of the lattice potential lies inside the confinement region, as explained in the main text of this article. This artificial boundary condition does not create a problem because we take $V_0 \gg gN/L$, so the function inside the lattice potential is exponentially small. In order to compute the stationary solution in the region where the potential is present, a numerical solution of the GP equation must be performed. In the situations considered in this article, $L \gg d$, so the wave function is very similar to that of the ideal confinement case. For numerical convenience, instead of fixing N and then obtaining the chemical potential, we first set n_0 to a typical experimental value of the density. Then, using $\mu_0 = gn_0$, we compute the number of particles, N , by integrating the resultant GP wave function. The computed number of particles satisfies $N/L = n_0 \left[1 + O(\xi_0/L) + O(d/L)\right]$.

A.3. Realistic optical lattice potential

In order to simulate a more realistic scenario, we introduce the following two potentials: on the left side, a Gaussian barrier centered at $x = 0$ of the form $V_L(x) = U \exp(-2x^2/w_L^2)$, with $w_L = 2 \mu\text{m}$, and on the right side, a realistic optical lattice centered at $x = L$, which has the form $V(x) = V_0 \cos^2[k_L(x - L)] \exp[-2(x - L)^2/\tilde{w}^2]$.

We take the amplitudes of the confining potentials to be much larger than the chemical potential. We also take $L \gg \tilde{w} \gg w_L$, so that they are well separated in space and there is a large region where the potential is negligible and where we expect some kind of flat wave function. The width, w_L , does not play a significant role in our simulations; we choose $w_L = 2 \mu\text{m}$. In this way, we can set $A(0) = 0$ and $A(L_{\text{bc}}) = 0$ as boundary conditions for the numerical computation, with L_{bc} sufficiently deep in the region where $V_0 \exp[-2(x-L)^2/\tilde{w}^2] \geq \mu_0$. Once we have fixed the potential and the boundary conditions for the numerical calculation, we repeat the same process of the previous subsection by fixing n_0 to a typical experimental value and using the resulting value of μ_0 to compute the number of particles, N .

Appendix B. Flowing condensate in a nonlinear optical lattice

The results of this section are partially based on [41]. The time-independent GP equation in an ideal *infinite* optical lattice whose potential has the same form as the long-time potential of equation (4), $V(x) = V_\infty \cos^2(k_L x)$, reads, after rescaling the wave function and the coordinates, $\Psi_0(z) \equiv \Psi(x)/\sqrt{n_r}$ (with $z \equiv 2k_L x$),

$$-\frac{1}{2} \frac{\partial^2 \Psi_0}{\partial z^2} + v \cos(z) \Psi_0 + c^2 |\Psi_0|^2 \Psi_0 = \alpha \Psi_0$$

$$v = \frac{V_\infty}{2E_L}, \quad c^2 = \frac{gn_r}{E_L}, \quad \alpha = \frac{\mu - V_\infty/2}{E_L}, \quad (\text{B.1})$$

where n_r is the average atomic density, μ is the chemical potential, and $E_L = 4\hbar^2 k_L^2/m = 8E_R$.

We look for solutions of the Bloch form

$$\Psi_0(z) = e^{iqz} y_q(z), \quad (\text{B.2})$$

with $y_q(z + 2\pi) = y_q(z)$ periodic, because the non-linear term is periodic for a Bloch-wave type solution. The normalization condition reads

$$\frac{1}{2\pi} \int_0^{2\pi} dz |\Psi_0(z)|^2 = 1. \quad (\text{B.3})$$

The Brillouin zone is placed in the region $-1/2 < q < 1/2$. The equation for y_q is:

$$-\frac{1}{2} \left(\frac{\partial}{\partial z} + iq \right)^2 y_q + v \cos(z) y_q + c^2 |y_q|^2 y_q = \alpha y_q, \quad (\text{B.4})$$

where we have allowed for a q -dependence of α , defined in (B.1). The linear (Schrödinger) regime is obtained when $c = 0$. For $c^2 > v$, some extra nonlinear Bloch waves appear. This generates a loop structure in the conduction band. In the systems analyzed in the present work, $c^2 \sim 10^{-3} - 10^{-4}$ and $v \sim 10^{-1}$, hence $v \gg c^2$. As a consequence, loops do not appear, and the system is close to the linear Schrödinger regime.

To compute the Bloch energy eigenvalues, we follow the method developed in [41]. First, we perform a finite Fourier expansion of the periodic function $y_q(z)$ of the form:

$$y_q(z) = \sum_{n=-M}^M c_n e^{inz}, \quad (\text{B.5})$$

where M is a numerically enforced cutoff. After substitution of this solution in (B.4) and in (B.3), we get $2M + 2$ equations for $2M + 2$ variables (the $2M + 1$ values of the Fourier coefficients, c_n , plus the eigenvalue, α). Instead of directly solving these nonlinear equations, it is more efficient to minimize the quadratic sum of the $2M + 2$ equations,

$$S = \sum_{j=1}^{2M+2} f_j^2, \quad (\text{B.6})$$

where $f_j(c_n, \alpha) = 0$ (with $j = 1, 2, \dots, 2M + 2$) are the equations to be solved. It is easy to see that all these equations are real, so the coefficients, c_n , can be chosen as real numbers and there is no need to use complex conjugates in (B.6).

A given Bloch solution can be unstable, either dynamically or in the sense of Landau, as explained below. The GP wave function is an extreme of the grand canonical Hamiltonian

$$K[\Psi(z), \alpha] = \int dz \left[\frac{1}{2} \left| \frac{\partial \Psi}{\partial z} \right|^2 + v \cos(z) |\Psi|^2 + \frac{c^2}{2} |\Psi|^4 - \alpha |\Psi|^2 \right]. \quad (\text{B.7})$$

A superflow through the lattice is obtained when the actual solution, $\Psi_0(z)$, minimizes the functional $K[\Psi(z), \alpha]$. When this is not the case, the system can minimize its energy by emitting excitations (phonons). The mean-field solutions of this last type are said to exhibit Landau instabilities. These instabilities can be sought by expanding $K[\Psi(z), \alpha]$ around $\Psi_0(z)$, (i.e., $\Psi(z) = \Psi_0(z) + \delta\Psi(z)$). The first-order term is automatically zero because $\Psi_0(z)$ solves the GP equation. The quadratic terms reads

$$\begin{aligned} \delta K &= \frac{1}{2} \int dz \left[\delta\Psi^* \delta\Psi \right] \Lambda \begin{bmatrix} \delta\Psi \\ \delta\Psi^* \end{bmatrix} \\ \Lambda &= \begin{bmatrix} H' & L \\ L^* & H' \end{bmatrix} \\ H' &= -\frac{1}{2} \frac{\partial^2}{\partial z^2} + v \cos(z) + 2c^2 |\Psi_0|^2 - \alpha_q \\ L &= c^2 \Psi_0^2. \end{aligned} \quad (\text{B.8})$$

Landau instabilities correspond to negative eigenvalues of the Hermitian operator, Λ . The corresponding eigenvalue equation is

$$\Lambda \begin{bmatrix} u \\ v \end{bmatrix} = \lambda \begin{bmatrix} u \\ v \end{bmatrix}. \quad (\text{B.9})$$

By absorbing the exponential plane-wave factor of the Bloch-type GP solution, $u(z) = e^{iqz} u_q(z)$ and $v(z) = e^{-iqz} v_q(z)$, we arrive at a new matrix operator, Λ_q , which is periodic. Applying Bloch's theorem in the form $u_q(z) = e^{ikz} u_{q,k}(z)$ and $v_q(z) = e^{ikz} v_{q,k}(z)$ with $u_{q,k}(z)$ and $v_{q,k}(z)$ periodic in $[0, 2\pi]$, the final eigenvalue equation reads

$$\begin{aligned}
\Lambda_{q,k} \begin{bmatrix} u_{q,k} \\ v_{q,k} \end{bmatrix} &= \lambda_{q,k} \begin{bmatrix} u_{q,k} \\ v_{q,k} \end{bmatrix} \\
\Lambda_{q,k} &= \begin{bmatrix} H''_{k+q} & L_q \\ L_q^* & H''_{k-q} \end{bmatrix} \\
H''_k &= -\frac{1}{2} \left(\frac{\partial}{\partial z} + ik \right)^2 + v \cos(z) + 2c^2 |y_q|^2 - \alpha \\
L_q &= c^2 y_q^2.
\end{aligned} \tag{B.10}$$

Dynamical instabilities correspond to modes that grow exponentially with time. They are computed by looking for nonreal eigenvalues of the BdG equations, which are formally similar to equation (B.9):

$$M \begin{bmatrix} u \\ v \end{bmatrix} = \epsilon \begin{bmatrix} u \\ v \end{bmatrix}, \tag{B.11}$$

with $M = \sigma_z \Lambda$ (here, $\sigma_z = \text{diag}(1, -1)$ is the usual Pauli matrix). Bloch's theorem also applies here, and after a computation similar to that which has led to equation (B.10), the eigenvalue equation reads

$$M_{q,k} \begin{bmatrix} u_{q,k} \\ v_{q,k} \end{bmatrix} = \epsilon_{q,k} \begin{bmatrix} u_{q,k} \\ v_{q,k} \end{bmatrix}, \tag{B.12}$$

with $M_{q,k} = \sigma_z \Lambda_{q,k}$. In addition to the dynamical stability analysis, the real eigenvalues of this operator can be used to compute the speed of sound in the optical lattice. When $q = 0$, it can be proven that the the small wave-vector k eigenvalues go like $\epsilon = \pm s |k|$, with s being the speed of sound (here, in units of $2\hbar k_L/m$). On the other hand, the form of the Bloch-type solution of the GP equation as a function of both q and n_r can be directly used to compute the sound speed without the need to solve for the BdG equations [31]. Restoring dimensions by introducing $Q = 2k_L q$, one can prove that

$$s = \frac{\sqrt{\partial_n^2 \mathcal{E} \partial_Q^2 \mathcal{E}}}{\hbar} \tag{B.13}$$

where ∂_n denotes derivative with respect the mean density, n_r , ∂_Q is the derivative with respect the pseudomomentum Q , with both derivatives evaluated at $Q = 0$, and \mathcal{E} is an average energy density given by

$$\begin{aligned}
\mathcal{E} &= \frac{n_r}{d} \int_0^d dx y_q^*(2k_L x) \left[-\frac{\hbar^2}{2m} \left(\frac{\partial}{\partial x} + iQ \right)^2 + V_\infty \cos^2(k_L x) \right. \\
&\quad \left. + \frac{gn_r}{2} |y_q(2k_L x)|^2 \right] y_q(2k_L x) \\
&= n_r \mu - \frac{gn_r^2}{4\pi} \int_0^{2\pi} dz |y_q(z)|^4.
\end{aligned} \tag{B.14}$$

We will make use of this expression in appendix C.

Appendix C. Perturbative treatment of the nonlinearity in the optical lattice

In this appendix, some of the results of appendix B are perturbatively explored further. In equation (B.1), there are two dimensionless parameters, v and c^2 . The former is essentially the amplitude of the potential ($v \gg 1$ is the tight-binding regime, while $v \ll 1$ corresponds to the nearly-free-particle regime) and the latter is a measure of the strength of the interaction or nonlinearity. In the cases studied in this paper, $v \ll 1$. However, the forthcoming discussion applies to arbitrary values of v . The quantity $\delta \equiv c^2 \ll 1$ is the small parameter of our perturbation theory. We expand in powers of δ both the Bloch wave, $y_q(z)$, and the displaced and dimensionless chemical potential α_q , which solves equations (B.3) and (B.4) and is defined in equation (B.1). We obtain

$$\begin{aligned} y_q(z) &= \sum_{m=0}^{\infty} \delta^m y_q^{(m)}(z), \\ \alpha_q &= \sum_{m=0}^{\infty} \delta^m \alpha_q^{(m)}, \end{aligned} \quad (\text{C.1})$$

which transforms equation (B.4) into (hereafter we omit the explicit z -dependence in $y_q(z)$, $y_q^{(m)}(z)$)

$$\begin{aligned} H_q^{(0)} y_q + \delta |y_q| y_q &= \alpha_q y_q \\ H_q^{(0)} &\equiv -\frac{1}{2} \left(\frac{\partial}{\partial z} + iq \right)^2 + v \cos(z). \end{aligned} \quad (\text{C.2})$$

In what follows, we focus on the lowest Bloch band and keep terms up to $O(\delta^2)$. The lowest-order term solves the linear Schrödinger equation, $H_q^{(0)} y_q^{(0)} = \alpha_q^{(0)} y_q^{(0)}$. Therefore, $y_q^{(0)} = \phi_{q,0}$ and $\alpha_q^{(0)} = \varepsilon_{q,0}$, where $\phi_{q,0}(z)$ is the corresponding eigenfunction for the lowest band, which involves Mathieu functions, and $\varepsilon_{q,0}$ is its eigenvalue (note the use of the index 0 for two different purposes: perturbative order is indicated in the superindex, while the band index comes in the subindex). We normalize $\phi_{q,0}$ according to (B.3).

The first-order corrections must satisfy

$$H_q^{(0)} y_q^{(1)} + |y_q^{(0)}|^2 y_q^{(0)} = \alpha_q^{(0)} y_q^{(1)} + \alpha_q^{(1)} y_q^{(0)}, \quad (\text{C.3})$$

which, using standard perturbation techniques, leads to

$$\begin{aligned} \alpha_q^{(1)} &= \frac{1}{2\pi} \int_0^{2\pi} dz |\phi_{q,0}|^4 \\ y_q^{(1)} &= \sum_{n=1}^{\infty} \beta_n \phi_{q,n} \\ \beta_n &= \frac{\frac{1}{2\pi} \int_0^{2\pi} dz \phi_{q,n}^* |\phi_{q,0}|^2 \phi_{q,0}}{\varepsilon_{q,0} - \varepsilon_{q,n}}, \end{aligned} \quad (\text{C.4})$$

where $\{\phi_{q,n}\}_{n=1}^{\infty}$ are the Schrödinger eigenvectors of the rest of bands and $\varepsilon_{q,n}$ are its corresponding eigenvalues, for a given value of q .

The second-order equation reads

$$H_q^{(0)}y_q^{(2)} + 2\left|y_q^{(0)}\right|^2 y_q^{(1)} + y_q^{(0)2}y_q^{(1)*} = \alpha_q^{(0)}y_q^{(2)} + \alpha_q^{(1)}y_q^{(1)} + \alpha_q^{(2)}y_q^{(0)}. \quad (\text{C.5})$$

We note that $y_q^{(2)}$ is not needed to compute $\alpha_q^{(2)}$. Specifically, we find

$$\begin{aligned} \alpha_q^{(2)} &= \frac{1}{2\pi} \int_0^{2\pi} dz \left| \phi_{q,0} \right|^2 \left(2\phi_{q,0}^* y_q^{(1)} + \phi_{q,0} y_q^{(1)*} \right) \\ &= -3 \sum_{n=1}^{\infty} \left| \beta_n \right|^2 (\varepsilon_{q,n} - \varepsilon_{q,0}), \end{aligned} \quad (\text{C.6})$$

which is always negative.

Instead of invoking Mathieu functions, the numerical computation of the formulae presented in this appendix (equations (C.4) and (C.6)) can be easily performed in a Fourier representation. As y_q , $\phi_{q,n}$ are periodic functions in $[0, 2\pi]$, their Fourier expansion reads $y_q(z) = \sum_{m=-\infty}^{\infty} c_m e^{imz}$ and $\phi_{q,n}(z) = \sum_{m=-\infty}^{\infty} a_{n,m} e^{imz}$. Both the c_m and the $a_{n,m}$ coefficients can be chosen to be real (see appendix B). In this Fourier representation, $H_q^{(0)}$ is a tridiagonal matrix with elements $\mathbf{H}_{m,m\pm 1} = v/2$ and $\mathbf{H}_{m,m} = (m+q)^2/2$. Multiplication by $|\phi_{q,0}|^2$ is represented by the matrix $\mathbf{r}_{m,p} = \sum_l a_{0,l} a_{0,l+m-p}$. The perturbative expansion of the Fourier components of solution to the GP equation reads $c_m = \sum_{n=0}^{\infty} \delta^n c_m^{(n)}$. In this Fourier basis, Mathieu's equation for all the bands is written as an eigenvalue-eigenvector matrix equation

$$\mathbf{H}\mathbf{a}_n = \varepsilon_{q,n} \mathbf{a}_n, \quad (\text{C.7})$$

where matrix multiplication is understood. The other previous results, equations (C.4) and (C.6) can be written as:

$$\begin{aligned} \alpha_q^{(1)} &= \mathbf{a}_0^\top \mathbf{r} \mathbf{a}_0 \\ \mathbf{c}^{(1)} &= \sum_{n=1}^{\infty} \beta_n \mathbf{a}_n \\ \beta_n &= \frac{\mathbf{a}_n^\top \mathbf{r} \mathbf{a}_0}{\varepsilon_{q,0} - \varepsilon_{q,n}} \\ \alpha_q^{(2)} &= 3\mathbf{a}_0^\top \mathbf{r} \mathbf{c}^{(1)} = -3 \sum_{n=1}^{\infty} \left| \beta_n \right|^2 (\varepsilon_{q,n} - \varepsilon_{q,0}). \end{aligned} \quad (\text{C.8})$$

Now we can use the perturbative results (C.8) to give approximate closed expressions for some parameters of the optical lattice. To the first order in δ , the energy density is given by equation (B.14),

$$\mathcal{E} \simeq n_r \left(\mu - \frac{gn_r}{2} \alpha_q^{(1)} \right). \quad (\text{C.9})$$

We can write

$$\begin{aligned}\mu &= E_L \alpha + \frac{V_\infty}{2} \simeq E_L \alpha_q^{(0)} + \frac{V_\infty}{2} + E_L \alpha_q^{(1)} \delta \\ &= \mu^{(0)} + E_L \alpha_q^{(1)} \delta,\end{aligned}\tag{C.10}$$

where E_L is defined after equation (B.1). On the other hand, for the noninteracting chemical potential, we have (assuming $q \ll 1/2$):

$$\mu^{(0)} = \mu^{(0)}(Q) \simeq E_{\min} + \frac{\hbar^2 Q^2}{2m^*},\tag{C.11}$$

where E_{\min} is the bottom of the conduction band as defined in the main text, m^* is the effective mass, and we recall that $Q = 2k_L q$. Thus we can rewrite equation (C.10) as:

$$\mu = E_{\min} + \frac{\hbar^2 Q^2}{2m^*} + g n_r \alpha_q^{(1)}.\tag{C.12}$$

Using (C.12), we can rewrite (C.9) as

$$\mathcal{E} \simeq n_r E_{\min} + n_r \frac{\hbar^2 Q^2}{2m^*} + \frac{g n_r^2}{2} \alpha_q^{(1)}.\tag{C.13}$$

Computing the derivatives to the lowest order in δ , we arrive at:

$$\begin{aligned}\frac{\partial^2 \mathcal{E}}{\partial Q^2} &\simeq n_r \frac{\hbar^2}{m^*}, \\ \frac{\partial^2 \mathcal{E}}{\partial n_r^2} &\simeq g \alpha_0^{(1)}.\end{aligned}\tag{C.14}$$

Now we compute the speed of sound using equation (B.13) and obtain:

$$s = \sqrt{\frac{g n_r}{m^*} \alpha_0^{(1)}} = \sqrt{\frac{g n_r}{m}} \sqrt{\frac{m}{m^*} \alpha_0^{(1)}}.\tag{C.15}$$

Similar results appear in [48] and references therein. The first square root is the speed of sound in the absence of the optical lattice. The second factor on the right takes into account the presence of the optical lattice and is practically unity for $v \ll 1$. Specifically, we can write:

$$\begin{aligned}m^* &= m \left(1 + 8v^2 + O(v^4) \right) \\ \alpha_q^{(1)} &= 1 + \frac{8v^2}{(1 - 4q^2)^2} + O(v^4),\end{aligned}\tag{C.16}$$

and then $\sqrt{m \alpha_0^{(1)} / m^*} = 1 + O(v^4)$, so $s \simeq \sqrt{g n_r / m}$, which is the usual expression for the speed of sound. Equation (C.15) can also be interpreted as the sound velocity arising in a system with an effective constant coupling, $g_{\text{eff}} = g \alpha_0^{(1)}$, and effective mass, m^* [49].

The current is also conserved for a stationary solution of the GP equation and is given, to the lowest order in δ and Q , by

$$j = \frac{1}{\hbar} \frac{\partial \mathcal{E}}{\partial Q} = n_r \frac{\hbar Q}{m^*}. \quad (\text{C.17})$$

In the nearly-free atom approximation, where the relative oscillations of the density around the mean value are small, we can write $j \simeq n_r \bar{v}$ where \bar{v} is a locally averaged flow velocity (not to be confused with the dimensionless parameter, v). Then, we have $\bar{v} \simeq \hbar Q / m^*$, and we can rewrite equation (C.12) in a more appealing form:

$$\mu = E_{\min} + \frac{1}{2} m^* \bar{v}^2 + m^* s^2. \quad (\text{C.18})$$

The physical interpretation of this equation is straightforward: the chemical potential in the optical lattice is the sum of the energy of the bottom of the conduction band plus the contribution of the kinetic energy and the interaction energy, both with m^* instead of m .

As explained at the end of appendix B, the same result for the speed of sound can be obtained by solving the BdG equations (B.12) perturbatively to the first order in δ . When $q = 0$, which implies that the GP solution $y_0(z)$ can be taken as real, we perform an expansion of the spinors in terms of solutions to the Schrödinger equation,

$$\begin{bmatrix} u_{0,k}(z) \\ v_{0,k}(z) \end{bmatrix} = \sum_{n=0}^{\infty} \phi_{k,n}(z) \chi_{k,n}, \quad (\text{C.19})$$

where $\chi_{k,n}$ are spinors of constant (z -independent) coefficients. The matrix operator, $M_{0,k}$, introduced in (B.12) can be written, to the first order in δ , as $M_{0,k} = M_k^{(0)} + M^{(1)}\delta$ with:

$$M_k^{(0)} = \begin{bmatrix} H_k^{(0)} - \varepsilon_{0,0} & 0 \\ 0 & -H_k^{(0)} - \varepsilon_{0,0} \end{bmatrix}$$

$$M^{(1)} = \begin{bmatrix} 2\phi_{0,0}^2(z) - \alpha_0^{(1)} & \phi_{0,0}^2(z) \\ -\phi_{0,0}^2(z) & -2\phi_{0,0}^2(z) + \alpha_0^{(1)} \end{bmatrix}, \quad (\text{C.20})$$

$\phi_{0,0}(z)$ being the Schrödinger solution for the bottom of the lowest band. Note that $\phi_{k,n}(z)$ are eigenfunctions of $H_k^{(0)}$. A matrix equation for the perturbative expansion of the $\chi_{k,0}$ spinors to the first order can be obtained by projecting onto the lowest Bloch eigenfunction, $\phi_{k,0}^*(z)$:

$\varepsilon(q=0, k)\chi_{k,0}$

$$= \begin{bmatrix} \varepsilon_{k,0} - \varepsilon_{0,0} + (2J(k) - \alpha_0^{(1)})\delta & J(k)\delta \\ -J(k)\delta & -\varepsilon_{k,0} + \varepsilon_{0,0} - (2J(k) - \alpha_0^{(1)})\delta \end{bmatrix} \chi_{k,0}$$

$$J(k) = \frac{1}{2\pi} \int_0^{2\pi} dz |\phi_{k,0}|^2 |\phi_{0,0}|^2. \quad (\text{C.21})$$

Restoring units for k by using $K = 2k_L k$, expanding to the lowest order near $K = 0$, and neglecting corrections $O(\delta)$ to m^* , the eigenvalues are approximated as

$$\epsilon(0, K) = \pm \left[\left(\frac{\hbar^2 K^2}{2m^*} \right)^2 + gn_r \alpha_0^{(1)} \frac{\hbar^2 K^2}{m^*} \right]^{\frac{1}{2}}, \quad (\text{C.22})$$

which for small K gives $\epsilon(0, K) \simeq \hbar s K$, with s given by (C.15).

The previous results can be used to compute the corrections to the width of the lowest band, which by using (C.21) leads to

$$\Delta_c^{\text{BdG}} \simeq \Delta_c + \left[2J(1/2) - \alpha_0^{(1)} \right] gn_r, \quad (\text{C.23})$$

where Δ_c is the Schrödinger bandwidth, and we have used $\Delta_c \gg gn_r$, which is true in all the situations considered in this paper.

Appendix D. Numerical methods: Crank–Nicolson method and absorbing boundary conditions

The numerical computation of the time evolution of the system was completed using the Crank–Nicolson method, as in [25]. The spatial interval, $[0, L_g]$, is divided into $N + 2$ equally spaced points separated by a distance, $\Delta x = L_g/(N + 1)$, and the time interval, $[0, t]$, into steps of size Δt . Hence, we write the grid points as

$$\begin{aligned} x_j &= j\Delta x \quad j = 0, 1 \dots N + 1 \\ t_k &= k\Delta t \quad k = 0, 1 \dots n. \end{aligned} \quad (\text{D.1})$$

Here, we use units such that $\hbar = m = \xi_0 = 1$, and rescale the wave function by extracting the factor, $\sqrt{n_0}$. The GP equation can be then written as

$$\begin{aligned} i \frac{\partial \Psi(x, t)}{\partial t} &= H(x, t) \Psi(x, t) \\ H(x, t) &= -\frac{1}{2} \frac{\partial^2}{\partial x^2} + V(x, t) + |\Psi(x, t)|^2 - 1 \end{aligned} \quad (\text{D.2})$$

where the ‘−1’ comes from subtracting the initial chemical potential and $V(x, t)$ is the time-dependent potential. Here, $H(x, t)$ plays the role of an effective Hamiltonian. If we define the spatial vector with the discretized values of the wave function in a given time, t_k , as Ψ_k , with components $\Psi_k^j = \Psi(x_j, t_k)$, and using

$$\begin{aligned} \Psi \left(x, t + \frac{\Delta t}{2} \right) &= \frac{\Psi(x, t + \Delta t) + \Psi(x, t)}{2} + O(\Delta t^2) \\ \frac{\partial \Psi}{\partial t} \left(x, t + \frac{\Delta t}{2} \right) &= \frac{\Psi(x, t + \Delta t) - \Psi(x, t)}{\Delta t} + O(\Delta t^2) \\ \frac{\partial^2 \Psi}{\partial x^2} (x, t) &= \frac{\Psi(x + \Delta x, t) + \Psi(x - \Delta x, t) - 2\Psi(x, t)}{\Delta x^2} + O(\Delta x^2), \end{aligned} \quad (\text{D.3})$$

potential (CAP) at the grid boundaries [50]. Instead of that, we make use of the alternative, so-called absorbing boundary conditions (ABC) [51, 52]. This method is based on the linearization of the dispersion relation in the boundary in order to achieve the relation corresponding to an outgoing plane wave. Both ABC and CAP are very useful because they not only prevent the artificial reflection of the waves, but also permit us to reduce the size of the supersonic zone.

The point $x = L_g$ is placed in the supersonic zone, where there is no potential. In addition, we expect that the nonlinear term in (D.2) can be neglected. This means that the effective Hamiltonian, H , in this region is the usual free (Schrödinger) Hamiltonian, and equation (D.2) can be written as

$$i \frac{\partial \Psi}{\partial t} = -\frac{1}{2} \frac{\partial^2 \Psi}{\partial x^2} - \Psi, \quad (\text{D.10})$$

which implies the dispersion relation

$$\omega = \frac{k^2}{2} - 1. \quad (\text{D.11})$$

On the supersonic side and in the quasi-stationary regime, the wave function is well peaked in momentum space around a value $k_0 \simeq \sqrt{2E_{\min}}$, where E_{\min} is the energy of the bottom of the first conduction band. By linearizing the dispersion relation around k_0 and expressing this relation in terms of derivatives, one can get

$$i \frac{\partial \Psi}{\partial t} = -ik_0 \frac{\partial \Psi}{\partial x} - \left(\frac{k_0^2}{2} + 1 \right) \Psi. \quad (\text{D.12})$$

We replace the hard-wall boundary condition at $j = N + 1$, equation (D.8), by the discrete version of equation (D.12) at $j = N$; hence there are $N + 1$ variables ($\Psi_k^j, j = 1 \dots N + 1$) and $N + 1$ equations corresponding to N equations resulting from equation (D.4) for $j = 1 \dots N$ and the ABC equation. We can regard the point x_{N+1} as a ghost point because the GP equation is not properly defined there and the ABC (D.12) is the corresponding equation for this point [52]. Following these considerations, we can easily implement the ABC condition by adding a new row to the matrices, M , which are now of size $(N + 1) \times (N + 1)$ and of the form

$$\mathbf{M}_{1,2} = \begin{bmatrix} \ddots & \ddots & & & \\ & \pm A & 1 \mp B_k^N & \pm A & \\ & \pm C & 1 \pm D & \mp C & \end{bmatrix} \quad (\text{D.13})$$

with

$$C = \frac{k_0 \Delta t}{4\Delta x}, \quad D = i \frac{\Delta t}{2} \left(\frac{k_0^2}{2} + 1 \right) \quad (\text{D.14})$$

Due to the finite size of the grid and the nonzero width of the momentum distribution in the supersonic region, the absorption is not perfect. We have found, however, that in practice, the small spurious reflections have no effect on the final results.

References

- [1] Garay L J, Anglin J R, Cirac J I and Zoller P 2000 *Phys. Rev. Lett.* **85** 4643

- [2] Chapline G, Laughlin R B and Santiago D I 2003 *Analog Models of General Relativity* ed M Visser (Singapore: World Scientific)
- [3] Unruh W 1976 *Phys. Rev. D* **14** 870
- [4] Unruh W G 1981 *Phys. Rev. Lett.* **46** 1351
- [5] Hawking S W 1974 *Nature* **248** 30
- [6] Hawking S W 1975 *Commun. Math. Phys.* **43** 199
- [7] Leonhardt U, Kiss T and Öhberg P 2003 *J. Opt. B* **5** S42
- [8] Leonhardt U, Kiss T and Öhberg P 2003 *Phys. Rev. A* **67** 33602
- [9] Balbinot R, Fabbri A, Fagnocchi S, Recati A and Carusotto I 2008 *Phys. Rev. A* **78** 21603
- [10] Carusotto I, Fagnocchi S, Recati A, Balbinot R and Fabbri A 2008 *New J. Phys.* **10** 103001
- [11] Macher J and Parentani R 2009 *Phys. Rev. A* **80** 43601
- [12] Finazzi S and Parentani R 2010 *New J. Phys.* **12** 095015
- [13] Lahav O, Itah A, Blumkin A, Gordon C, Rinott S, Zayats A and Steinhauer J 2010 *Phys. Rev. Lett.* **105** 240401
- [14] Recati A, Pavloff N and Carusotto I 2009 *Phys. Rev. A* **80** 43603
- [15] Zapata I, Albert M, Parentani R and Sols F 2011 *New J. Phys.* **13** 63048
- [16] Larré P E, Recati A, Carusotto I and Pavloff N 2012 *Phys. Rev. A* **85** 13621
- [17] Finazzi S and Carusotto I 2014 *Phys. Rev. A* **90** 033607
- [18] de Nova J R M, Sols F and Zapata I 2014 *Phys. Rev. A* **89** 043808
- [19] Busch X and Parentani R 2014 *Phys. Rev. D* **89** 105024
- [20] Steinhauer J 2014 *Nat. Phys.* **10** 864
- [21] Kamchatnov A M and Pavloff N 2012 *Phys. Rev. A* **85** 33603
- [22] Gerace D and Carusotto I 2012 *Phys. Rev. B* **86** 144505
- [23] Bloch I, Hänsch T W and Esslinger T 1999 *Phys. Rev. Lett.* **82** 3008
- [24] Andersson E, Calarco T, Folman R, Andersson M, Hessmo B and Schmiedmayer J 2002 *Phys. Rev. Lett.* **88** 100401
- [25] Paul T, Hartung M, Richter K and Schlagheck P 2007 *Phys. Rev. A* **76** 63605
- [26] Guerin W, Riou J-F, Gaebler J P, Josse V, Bouyer P and Aspect A 2006 *Phys. Rev. Lett.* **97** 200402
- [27] Gattobigio G L, Couvert A, Jeppesen M, Mathevet R and Guéry-Odelin D 2009 *Phys. Rev. A* **80** 041605
- [28] Vermersch F, Fabre C M, Cheiney P, Gattobigio G L, Mathevet R and Guéry-Odelin D 2011 *Phys. Rev. A* **84** 043618
- [29] Brantut J-P, Meineke J, Stadler D, Krinner S and Esslinger T 2012 *Science* **337** 1069
- [30] Brantut J-P, Grenier C, Meineke J, Stadler D, Krinner S, Kollath C, Esslinger T and Georges A 2013 *Science* **342** 713
- [31] Pethick C J and Smith H 2008 *Bose–Einstein condensation in Dilute Gases* (Cambridge: Cambridge University Press)
- [32] Pitaevskii L and Stringari S 2003 *Bose–Einstein Condensation* (Oxford: Clarendon)
- [33] Menotti C and Stringari S 2002 *Phys. Rev. A* **66** 043610
- [34] Leboeuf P and Pavloff N 2001 *Phys. Rev. A* **64** 033602
- [35] Petrov D S, Shlyapnikov G V and Walraven J T M 2000 *Phys. Rev. Lett.* **85** 3745
- [36] Dunjko V, Lorent V and Olshanii M 2001 *Phys. Rev. Lett.* **86** 5413
- [37] Zapata I and Sols F 2009 *Phys. Rev. Lett.* **102** 180405
- [38] Fabre C M, Cheiney P, Gattobigio G L, Vermersch F, Faure S, Mathevet R, Lahaye T and Guéry-Odelin D 2011 *Phys. Rev. Lett.* **107** 230401
- [39] Blakie P B, Ballagh R J and Gardiner C W 2002 *Phys. Rev. A* **65** 033602
- [40] Abramowitz M 1988 *Am. J. Phys.* **56** 958
- [41] Wu B and Niu Q 2003 *New J. Phys.* **5** 104
- [42] Cheiney P, Damon F, Condon G, Georgeot B and Guéry-Odelin D 2013 *Europhys. Lett.* **103** 50006

- [43] Cheiney P, Fabre C M, Vermersch F, Gattobigio G L, Mathevet R, Lahaye T and Guéry-Odelin D 2013 *Phys. Rev. A* **87** 013623
- [44] Carusotto I and La Rocca G C 2000 *Phys. Rev. Lett.* **84** 399
- [45] Santos L and Roso L 1998 *Phys. Rev. A* **58** 2407
- [46] Santos L and Roso L 1999 *Phys. Rev. A* **60** 2312
- [47] Byrd P F and Friedman M D 1971 *Handbook of Elliptic Integrals for Engineers and Scientists* (Berlin: Springer)
- [48] Krämer M, Menotti C, Pitaevskii L and Stringari S 2003 *Eur. J. Phys. D* **27** 247
- [49] Carusotto I, Embriaco D and La Rocca G C 2002 *Phys. Rev. A* **65** 053611
- [50] Muga J G, Palao J P, Navarro B and Egusquiza I L 2004 *Phys. Rep.* **395** 357
- [51] Xu Z and Han H 2006 *Phys. Rev. E* **74** 37704
- [52] Zhang J, Xu Z and Wu X 2008 *Phys. Rev. E* **78** 26709